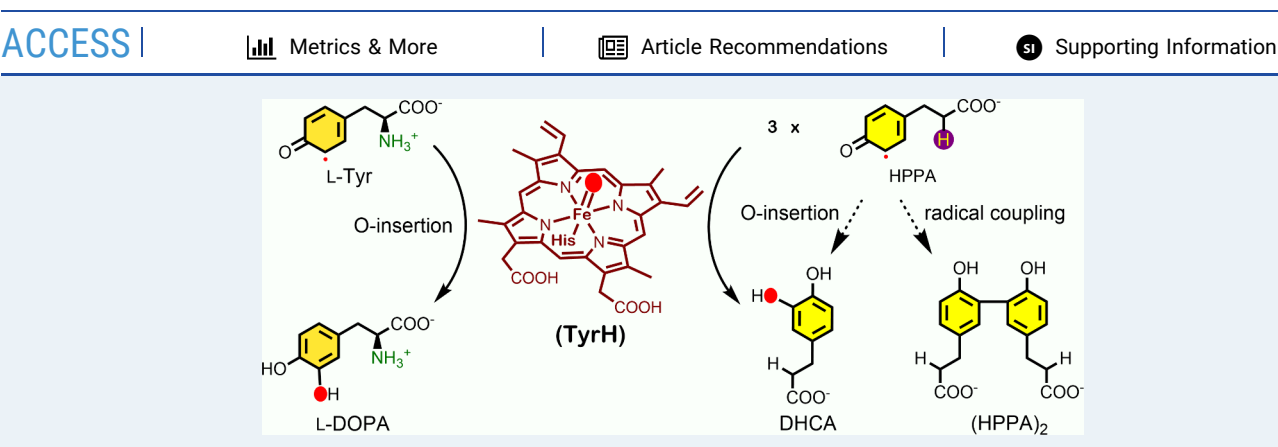


pubs.acs.org/acscatalysis Research Article

Substrate Analogs Implicate a Free Radical Pathway in Tyrosine Hydroxylase Catalysis

Ephrahime S. Traore, Yifan Wang, Wendell P. Griffith, and Aimin Liu*





ABSTRACT: Heme-dependent tyrosine hydroxylases (TyrH) are critical enzymes in catecholamine biosynthesis, yet the role of the substrate's α -amino group in their monooxygenation mechanism has been unclear. Using 3-(4-hydroxyphenyl)propionic acid (HPPA), an L-tyrosine analog lacking the α -amino group, we observed a distinct dimerization pathway that competes with the expected hydroxylation reaction. Several lines of evidence confirm that this process originates from a radical intermediate. First, the formation of this (HPPA)₂ dimer is selectively inhibited by a free radical scavenger. Second, ¹⁸O-labeling experiments show phenolic oxygen scrambling, indicating a disruption of substrate aromaticity during catalysis. Finally, EPR spectroscopy using nitrosobenzene as a substrate analog revealed a substrate-based free radical. This mechanistic divergence clarifies the role of the α -amino group. Its absence in HPPA creates a kinetic bottleneck for the final O atom transfer step, allowing a fraction of the substrate radical to form the off-pathway dimer. Thus, the native substrate's α -amino group acts as a crucial kinetic modulator, ensuring the rapid and efficient commitment of the substrate radical to productive hydroxylation. These results collectively establish a peroxidase-like free radical pathway for TyrH and reveal the nonessential yet significant role the amino group plays in controlling reaction outcomes.

KEYWORDS: Heme, Oxygenation, Intermediate, Radical spin-trap, Electron paramagnetic resonance, Resonance Raman, X-ray crystallography, Enzyme kinetics

■ INTRODUCTION

Oxidation of L-tyrosine (L-Tyr) to L-3,4-dihydroxyphenylalanine (L-DOPA) is a critical step in the metabolism of aromatic molecules across diverse life forms. 1-5 Catecholamines, such as L-DOPA, are known to enhance bacterial growth, and understanding their mechanism would be beneficial to human health. Additionally, L-DOPA has the unique ability to cross-link and form biological polymers found in mussel foot proteins, tubeworm adhesive, and squid beak polymer. TyrHs from different metabolic pathways canonically employ either a nonheme iron for an O2-dependent oxidation process using tetrabiopterin as cosubstrate⁸ or binuclear copper⁹ as the metallocofactor. However, a new class of heme-dependent TyrH using H2O2 as an oxidant has recently emerged, expanding the known repertoire of TyrH enzymes (Scheme 1A). 10-16 These TyrH proteins are responsible for the initial step in the biosynthesis of several natural products with antibacterial and antitumor properties, some of which include

anthramycin, lincomycin, hormaomycin, porothramycine, saframycin, sibiromycin, and tomaymycin. 11,12,17–20 Notably, these natural products contain a pyrroline moiety, which is derived from the product of the TyrH reaction. The discovery of these heme-dependent TyrHs highlights the distinct cofactor versatility in enzyme-mediated L-DOPA formation.

The heme-containing TyrHs belong to the recently defined histidine-ligated heme-dependent aromatic oxygenase (HDAO) superfamily. This functionally related superfamily, characterized by a shared core structure, has emerged from a significant expansion of the tryptophan-2,3-dioxygenase

Received: August 15, 2025 Revised: September 25, 2025 Accepted: October 7, 2025



Scheme 1. General Scheme of TyrH Reaction with L-Tyr (A), Scheme with 3-F-L-Tyr (B), and Structure of 3-(4-hydroxyphenyl)propionic Acid (HPPA) (C)

(TDO) family, incorporating monooxygenase members with tyrosine and its metabolites as substrates. Currently, this expanding superfamily encompasses several hundred members, collectively enriching our understanding of metalloenzymemediated oxygenation reactions, particularly in contrast to well-characterized heme-thiolate enzymes like cytochromes P450 and peroxygenases. Insights gleaned from the HDAO superfamily will hold promise for applications in metabolism and natural product biosynthesis.

In the past five years, considerable progress has been made toward characterizing these heme-dependent TyrHs. As a result, these enzymes have been shown, in addition to activating C-H bonds for hydroxylation, to activate C-F bonds for cleavage under mild conditions when fluorinated tyrosine is used as an alternate substrate in catalysis (Scheme 1B). TyrH from Streptomyces sclerotialus has been successfully crystallized in the substrate-bound form allowing us to experimentally identify an active site acid-base catalyst, His88. 13 A heme-bound hydroperoxo intermediate, also known as compound 0 (cpd 0) in heme chemistry, has been captured and structurally determined through in crystallo reactions with the alternate substrate 3-fluoro-L-tyrosine (3-F-L-Tyr). 14 This structure provided valuable insights into the catalytic mechanism of TyrH and paved the way for further studies on its reactivity and applications.

The above advancements in elucidating the three-dimensional structure and spectroscopic characteristics of heme-dependent TyrH have spurred two independent computational studies. A QM/MM study not only supported the catalytic role of His88 but also revealed the significance of the heme propionate group, which promotes catalytic steps by affecting the intrinsic electric fields of the distal pocket. Another molecular dynamic simulation supports the experimental finding of substrate conformation dictating aromatic C–H versus C–F bond activation when both F and H are present in 3-F-L-Tyr during TyrH-mediated catalysis. 16

In the crystal structure of the binary enzyme—substrate (ES) complex, the L-Tyr substrate bound at the distal heme pocket establishes extensive interactions with residues in the second-coordination sphere of the distal pocket of the heme. Intriguingly, the amino group of the bound substrate does not directly engage with protein residues or the heme cofactor but instead forms hydrogen bonds with well-ordered water

molecules in proximity. These water molecules, in turn, interact with the propionate group of the histidyl-ligated heme, which extends into the heme distal pocket. Remarkably, the 1.58 Å-resolution crystal structure of the ferric-hydroperoxide intermediate reveals the distal oxygen of the Fe^{III}—OOH is H-bonded with the amino group of the bound substrate, the amide backbone of Gly158, and is in close contact with the propionate group pointing toward the distal pocket.¹⁴ Furthermore, the amino group of the substrate interacts with both atoms of the hydroperoxide ligand. However, the impact of the interaction between the amino group and hydroperoxo ligand on catalysis remains unassessed in previous experimental and computational studies.

This work aims to compare dioxygenase and monooxygenase mechanisms to determine how the differences between HDAO members have affected their enzymatic function as well as to identify the main factors that control oxygen transfer to the substrate. TDO, the most studied founding member, is integral to the primary catabolic pathway of L-tryptophan (L-Trp) degradation, catalyzing the conversion of L-Trp to Nformyl-kynurenine, a pivotal step in this metabolic process. Recent experimental and computational studies have elucidated the intricate oxygen transfer mechanism from molecular dioxygen to L-Trp. Notably, a special aspect of the TDO catalytic pathway is that the amino group of the substrate, L-Trp, facilitates the second O atom transfer step during oxygenation. 22-25 This finding is potentially applicable to aromatic oxygenation mediated by other members of the HDAO superfamily. Hence, we are intrigued to explore whether the amino group of the substrate also plays a role in tyrosine oxidation catalyzed by heme-dependent TyrH, the prototype of an HDAO subclass where only one oxygen is inserted into the aromatic substrate. Typically, mutation on key residues is employed to study substrate-protein interactions and their mechanistic implications. However, this invites unwanted protein structural changes, further complicating the mutagenesis results. Thus, we employed 3-(4-hydroxyphenyl)propionic acid (HPPA) as an alternate substrate, which is structurally similar to L-Tyr but lacks the amino group (Scheme 1C). This is akin to mutation of the substrate without disruption of protein folding. Our findings with HPPA, coupled with hydroxyurea and another alternate substrate, nitrosobenzene, highlight the first substrate-based

intermediate captured in the monooxygenation reaction catalyzed by the HDAO superfamily, providing valuable mechanistic insights into the heme-dependent tyrosine hydroxylation.

RESULTS

Characterization of TyrH-Mediated HPPA Oxidation. When HPPA was used in place of L-Tyr as an alternate substrate in the established catalytic assay, 13,14 two reaction products were observed in the HPLC chromatogram (Figure 1A). Briefly, the assay was conducted by incubating excess L-Tyr, or HPPA, with TyrH for 5 min before H2O2 was slowly titrated into the mixture. The first product, which eluted at 8.78 min, had an m/z value of 181.0507 (0.55 ppm) as determined by high-resolution mass spectrometry (HRMS). This product was undetectable in positive ion mode but readily identifiable in negative ion mode by electrospray ionization n mass spectrometry. Consequently, all HRMS data for the substrate and its related products were acquired in the negative ion mode. Compared to HPPA, which has a retention time of 10.29 min and an m/z value at 165.0557 (0.11 ppm), this first product exhibits a 16 Da mass increase, consistent with the expected oxygen insertion product, dihydrocaffeic acid (DHCA). Surprisingly, another product, the third elution peak at 12.38 min with an m/z value at 329.1034 (1.03 ppm), was detected. This fraction was consistent with the molecular weight of the dimerized substrate. Because the two HPPA molecules could be cross-linked in various ways, such as at the

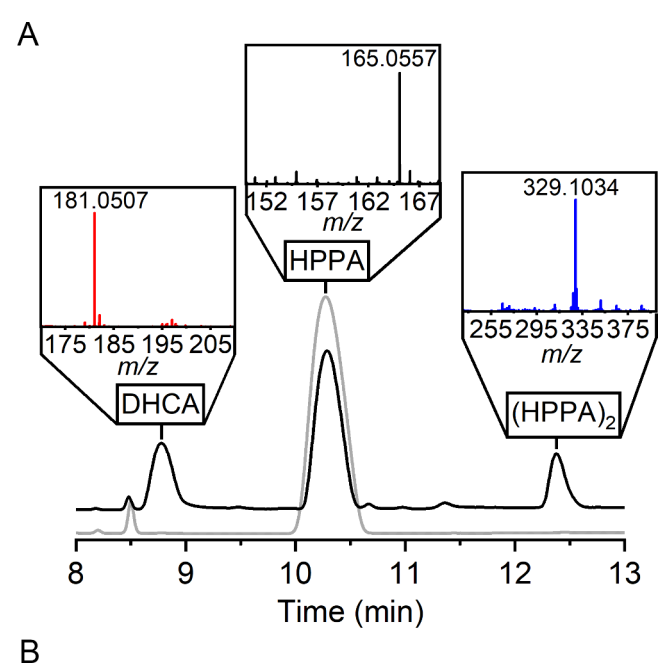
We employed proton NMR spectroscopy to ascertain the chemical structures of the products. The 1H NMR spectrum for HPPA (Figure S1) contains two distinct methylene triplets at 2.87 and 2.65 ppm, both with J=7.4 Hz. These protons have been assigned in the figure as H_{β} and H_{α} , respectively. The aromatic region consists of two doublets, one at 7.19 ppm and another at 6.85 ppm with J=8.2 Hz, which aligns with an expected *ortho* coupling (Figure 1B, black trace). These peaks represent two sets of equivalent protons, one pair as H_{6} and H_{2} , and the other as H_{5} and H_{3} . These spectroscopic data are consistent with the known spectroscopic fingerprints of HPPA. 26

aromatic rings, the hydroxyl groups, or a combination of the two, further validation and structure determination were

required for product identification.

The 1 H NMR spectrum of the expected hydroxylated DHCA product also contains two triplet peaks corresponding to the methylene protons (Figure S2). The signals in the aromatic region (Figure 1B, red trace) shifted upfield due to the presence of the electron-donating hydroxyl group. This region exhibits a doublet of doublets at 6.73 ppm with J=7.9 and 2.2 Hz, which is indicative of *ortho* and *meta* couplings, respectively, a doublet at 6.83 ppm with J=2.1 Hz, and a doublet at 6.87 ppm with J=8.1 Hz. There is now a loss of one equivalent set, the H_5 and H_3 , due to hydroxylation occurring at the C3 position. These results match well with the aromatic region of the 1 H NMR spectrum of L-DOPA. 13

The alkyl region of (HPPA)₂ (Figure S3) is consistent with HPPA and DHCA, indicating no new C–C bond at the C_{α} or C_{β} position. The aromatic region (Figure 1B, blue trace), which has shifted downfield due to the electron-withdrawing nature of the phenol group, is composed of a doublet of doublets at 7.21 ppm with J=8.3 and 2.2 Hz. These indicate an *ortho* and *meta* coupling. A doublet at 7.14 ppm with J=2.3 Hz is suggestive of *meta* coupling, and a doublet at 6.96 ppm



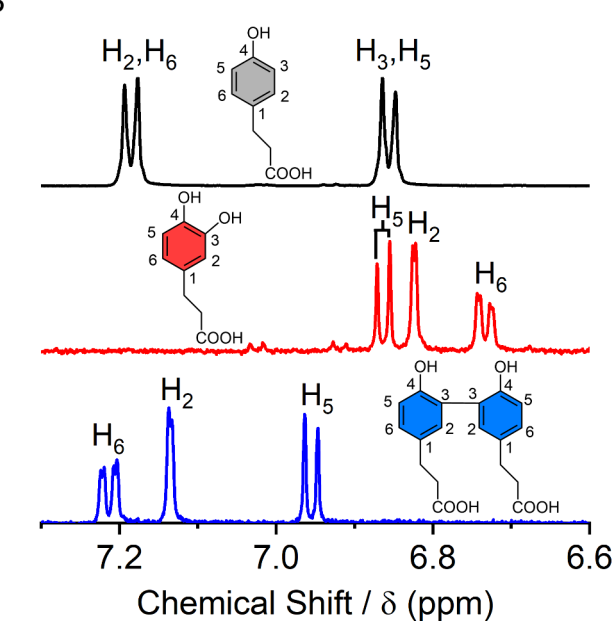


Figure 1. Product characterization of TyrH-mediated HPPA oxidation. (A) HPLC chromatogram of TyrH (100 μ M) with HPPA (2 mM, gray) and in the presence of 20 eq of H₂O₂ (black) monitored at 280 nm. The inset is the HRMS spectra measured in the negative mode of DHCA (red), HPPA (black), and (HPPA)₂ (blue). (B) NMR spectra of purified product peaks by HPLC from panel A. The corresponding chemical structures are provided for each spectrum. HPPA, DHCA, and (HPPA)₂ are represented in gray, red, and blue, respectively. Aromatic carbon positions are labeled 1 through 6.

with J=8.3 Hz represents *ortho* coupling. Due to the radical density known for tyrosyl radical, it is expected that carbon–carbon coupling would take place at C3. Additional HMBC and HSQC data were obtained and support dimerization at the C3 position (Figure S4 and Table S1). NMR analysis coupled with HRMS unequivocally facilitates the assignment of the chemical structure of the 329.1034 m/z product eluted at 12.43 min to 3,3'-(6,6'-dihydroxy-[1,1'-biphenyl]-3,3'-diyl)-dipropionic acid, henceforth denoted as (HPPA)₂. The

substantial presence of the (HPPA)₂ product implies a radical-based dimerization occurring during the TyrH-mediated reaction employing this alternate substrate.

¹⁸O-Labeled Study of TyrH and HPPA. Our prior investigations, utilizing isotopically labeled oxygen on substrates, yielded crucial mechanistic insights into the formation of L-DOPA. ¹³ Notably, oxygen scrambling at the C3 and C4 position of L-DOPA was observed, indicating a substrate-based radical forms during the catalytic cycle. Building upon this foundation, we adopted a comparable methodology to probe whether the formation of DHCA and (HPPA)₂ entails the presence of a longer-lived intermediate for solvent exchange in contrast to L-Tyr. Following the termination of the reaction with concentrated hydrochloric acid and subsequent purification via HPLC, each chromatographic peak underwent meticulous analysis using HRMS.

In the mass spectrometry analysis with $\mathrm{H_2}^{18}\mathrm{O}$, the HPPA peak displayed an expected m/z of 165.0553 with a 2.42 ppm error. Notably, two additional peaks at m/z values of 167.0596 (2.17 ppm) and 169.0639 (1.82 ppm) were observed, both showing an increase of 2 and 4 Da, respectively. This result suggests ¹⁸O-isotopic enrichment of one and two of the oxygens, respectively (Figure 2A). The ratios of unlabeled,

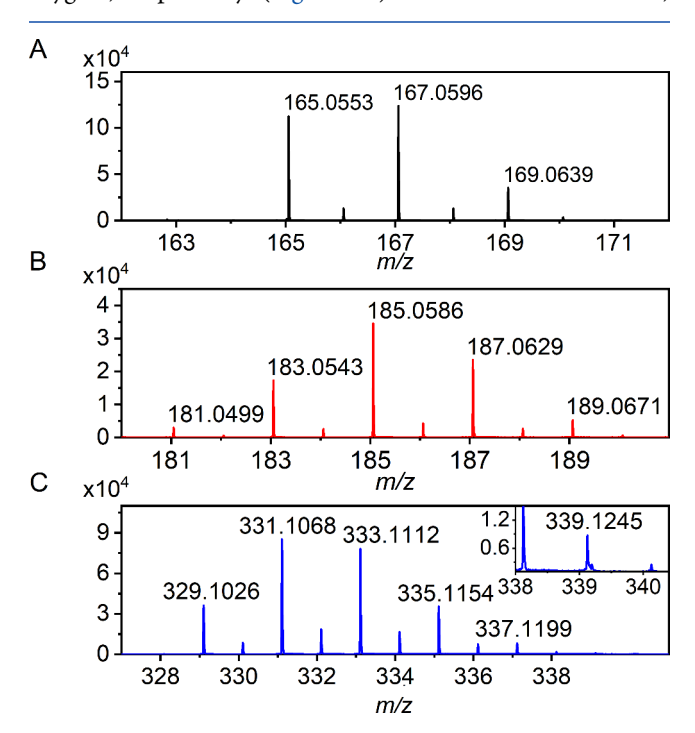


Figure 2. High-resolution mass spectrometry analyses of the reaction in the buffer with ¹⁸O-enriched H₂O. Isotope distribution of (A) HPPA (black), (B) DHCA (red), and (C) (HPPA)₂ (blue). The inset in panel C is a zoom in on the peak at 339.1245 m/z.

singly labeled, and doubly labeled (in both the original phenolic oxygen of the substrate and the newly inserted oxygen) hydroxylation products were 32.9%, 59.6%, and 7.5%, respectively (Table S2). To determine the location of these enriched ¹⁸O atoms, as HPPA also contains a carboxylate group, fragmentation analysis was performed (Figure S5A). The analysis revealed no oxygen exchange occurring at the hydroxyl group of the phenol nor 4-ethylphenol fragments. Hence, the observed scrambling is derived from the carboxylate of HPPA (Figure S6A). This observation is

consistent with a phenomenon observed in 4-hydroxyphenyl-pyruvate dioxygenase, where the carboxyl group can exchange with the bulk solvent in the absence of the amino group.²⁷

Carboxylic oxygen exchange with solvent was also observed with DHCA and (HPPA)₂ (Figure S6 B & C). DHCA has an expected m/z of 181.0499 (3.87 ppm), with up to four isotopically labeled product peaks detected with m/z values of 183.0542 (3.15 ppm), 185.0586 (2.82 ppm), 187.0629 (2.50 ppm), and 189.0671 (2.71 ppm), corresponding to 2, 4, 6, and 8 Da increases, respectively (Figure 2B). Fragmentation confirmed ¹⁸O enrichment at both hydroxyl groups of the 4-ethylcatechol end of DHCA (Figure S5B).

(HPPA)₂ has an expected m/z of 329.1026 (1.52 ppm) with up to five isotopically labeled oxygen atoms detected at m/z values of 331.1068 (1.53 ppm), 333.1112 (1.06 ppm), 335.1154 (1.18 ppm), 337.1199 (0.42 ppm), and 339.1243 (0.63 ppm), consistent with 2, 4, 6, 8, and 10 Da increases, respectively (Figure 2C). Fragmentation of these peak values reveals ¹⁸O-enrichment at three of the four possible oxygen atoms, including the phenolic oxygen position (Figure SSC).

Tables S2 and S3 summarize the ratios of isotopically labeled and nonlabeled peaks for DHCA and (HPPA)₂. Despite complications in the analysis due to carboxylic scrambling, the detection of oxygen scrambling on the original phenolic oxygen of the substrate suggests a common mechanism similar to the production of L-DOPA in the L-Tyr oxidation between the formation of DHCA and (HPPA)₂. Thus, it is reasonable to propose that the broken aromaticity determined with L-Tyr also applies to HPPA. A radical-based intermediate is expected to form during the production of (HPPA)₂. In the L-Tyr reaction, this intermediate is even shorter-lived based on the absence of dimerization. Therefore, further investigation using spectroscopy is needed to clarify the differences between HPPA and L-Tyr.

Spectroscopic Characterization of TyrH-HPPA Interaction. The UV-vis spectrum of TyrH exhibits a Soret band at 405 nm with α/β bands at 535 and 503 nm, respectively, and a charge transfer band at 636 nm (Figure S7A). In the presence of excess L-Tyr, no significant changes occur in the heme electronic states within the Soret, α/β , or charge transfer bands. The heme center of TyrH exhibits a S = 5/2 axial EPR signal with a g_{\perp} at 5.77 and a g_{\parallel} at 2.00 (Figure S7B). Once bound with L-Tyr, a minor decrease in high-spin signal is observed, and a new low-spin species is detected with g-values at 2.71, 2.22., and 1.76 (Figure S7C, red trace). With excess HPPA, a minor species with a weak g = 6.18 resonance suggests a heterogeneous iron center. However, no low-spin signal is detected (Figure S7C, blue trace). The $K_{\rm M}$ values for both tyrosine and HPPA were comparable (Figure S8). Overall, neither ligand coordinates to the iron, and only minor differences in the iron environment were noted between L-Tyr-bound and HPPA-bound TyrH.

We further characterized the binary complex using resonance Raman (rR) spectroscopy (Figure 3). The high-frequency region, dominated by the porphyrin in-plane vibrational modes, provides markers indicating the spin and oxidation state of the heme iron center. The ν_2 mode (1550–1600 cm⁻¹) is sensitive to the spin-state of the heme iron, and the ν_3 mode (1475–1520 cm⁻¹) is responsive to both the spin-state and the axial coordination. ^{28–30} Additionally, the strong ν_4 mode (1350–1400 cm⁻¹) is influenced by the oxidation state of the heme iron π -electron density of the porphyrin macrocycle. In the low-frequency region (200–1000 cm⁻¹), we

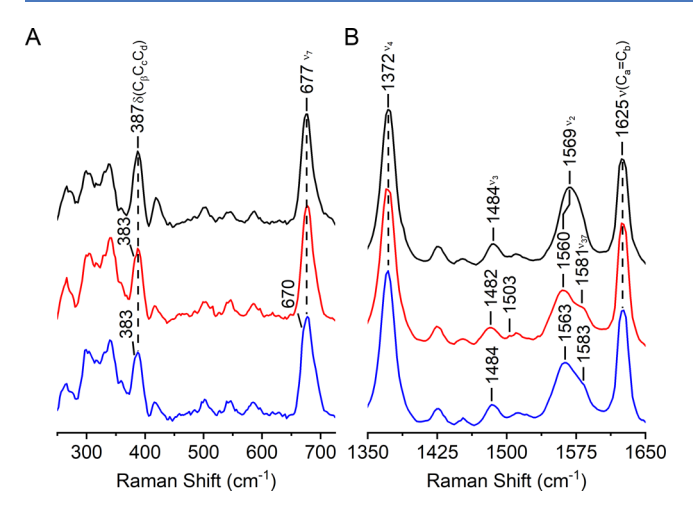


Figure 3. Resonance Raman spectra of ferric TyrH (black trace) bound with L-Tyr (red) and HPPA (blue) with a laser excitation wavelength of 406.7 nm in the low-frequency region (A) and high-frequency region (B).

gain structural insights related to iron-ligand interactions and heme out-of-plane modes. The high-frequency region (Figure 3B) of substrate-free TyrH indicates a ferric six-coordinate high-spin (6cHS) species with stretches at 1484 cm⁻¹ and 1569 cm⁻¹. When excess L-Tyr is present, a 2 cm⁻¹ shift in the ν_3 marker is paired with a 9 cm⁻¹ downshift in the ν_2 region, which are still consistent with a 6cHS species. Furthermore, a new minor peak at 1503 cm⁻¹ emerges, indicative of a new six-coordinate low-spin species, corroborated by the EPR spectrum. The major difference in the low-frequency region (Figure 3A) is a new feature at 383 cm⁻¹, suggesting movement in the propionate group in response to binding of L-Tyr.

TyrH-HPPA displays a ν_2 peak shift to 1563 cm⁻¹ and the concomitant loss of the six-coordinate low spin marker in the ν_2 region, consistent with EPR spectroscopy. In the presence of substrate or alternate substrate, the heme iron remains predominantly as a 6cHS species. Similar to tyrosine-bound TyrH a shoulder is seen at 383 cm⁻¹. Although active site reorganization is detected in response to substrate and alternate substrate binding, overall, the TyrH-HPPA complex exhibits similar spectroscopic features as TyrH bound with L-Tyr.

Crystal Structure Determination of TyrH-HPPA Complex. We obtained an ES complex structure of HPPA-bound TyrH refined to 1.56-Å resolution (PDB entry: 8VMK, Table S4), with two identical polypeptides in an asymmetric unit. The overall structure is nearly identical to the L-Tyr-bound TyrH complex, with a root-mean-square deviation value of 0.23 Å for 603 C α (Figure S9). However, the absence of the amino group in HPPA results in notable differences in the distal pocket (Figure 4). The HPPA-bound structure reveals one subunit containing a water molecule while another has two water molecules in the distal heme pocket. This heterogeneity was recognized by EPR spectroscopy and explains why a new high-spin species is detected in the TyrH-HPPA complex. In contrast, both subunits of the L-Tyr-bound TyrH complex (PDB: 7KQR) have two well-ordered water molecules in nearly equivalent positions in the distal heme pocket with an H-bond network connecting the heme iron with the bound L-Tyr substrate. Although minor differences were detected

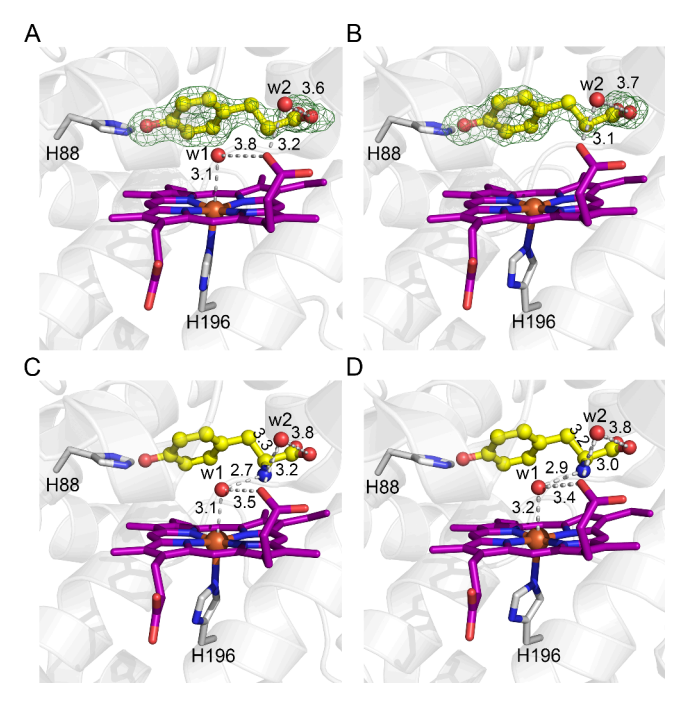


Figure 4. Active site view of TyrH in complex with L-Tyr and HPPA. (A) Chain A and (B) B of TyrH-HPPA (PDB entry: 8VMK), with HPPA shown in yellow as ball and sticks. The green $F_{\rm O}$ - $F_{\rm C}$ omit map is contoured to 3 σ . (C) Chain A and (D) B of TyrH-Tyr (PDB ID: 7KQR), with L-Tyr shown in yellow as ball and sticks. Enzymatic carbons are shown in gray, with distal histidine 196 and 88 as sticks and heme carbons as purple. Gray dashed lines indicate distances between atoms.

between the L-Tyr- and HPPA-bound structures, both similarly bind to TyrH, which is consistent with our spectroscopic data.

Characterization of a Spin-Trapped Free Radical Species. To investigate the anticipated radical-based mechanism suggested by HPPA oxidation, we employed hydroxyurea (HU), a well-known free radical scavenger for enzymatic reactions. $^{31-34}$ HU does not absorb at 288 nm nor does it react with TyrH mixed with $\rm H_2O_2$; thus, no product was detected by HPLC (Figure 5, i, ii, iii). In the presence of excess HU, the dimerized product is abolished (Figure 5, v). We quantitated the relative amount of substrate and product by combining the peak areas of DHCA, HPPA, and (HPPA)2 and

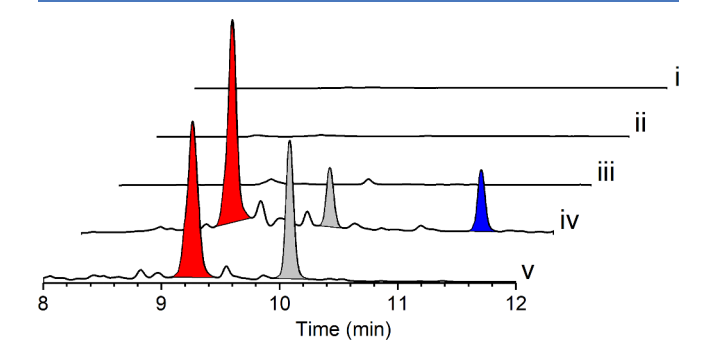


Figure 5. Activity assay with hydroxyurea. HPLC of (i) HU, (ii) HU mixed with H_2O_2 , (iii) TyrH incubated with HU and H_2O_2 , (iv) TyrH-HPPA complex mixed with H_2O_2 , and (v) TyrH-HPPA complex mixed with HU and H_2O_2 . Peaks shaded in red, gray, and blue correspond to DHCA, HPPA, and (HPPA)₂, respectively. All chromatograms were monitored at 288 nm.

dividing them by the respective peak areas. This method allows us to determine percentages of 65.4 \pm 3%, 18.5 \pm 1.7%, and $16.1 \pm 1.4\%$ for DHCA, HPPA, and (HPPA)₂, respectively, for the uninhibited reaction (Figure 5, (iv). In the presence of HU, these percentages shift to 57.9 \pm 0.2%, 41.6 \pm 0.1%, and 0.42 \pm 0.09% (Figure 5, (v). HU not only eradicates the formation of (HPPA), but also results in a slight decrease of the hydroxylated product. Mixing excess HU with TyrH shows no significant shifts in the UV-vis spectrum (Figure S10), indicating that HU does not cause substantial reorganization in the active site. Plotting the formation rates of DHCA and (HPPA)₂, monitored at 280 and 288 nm respectively, against HU concentration shows a clear decrease in rate with increasing HU, consistent with the HPLC results (Figure S11). The attenuated (HPPA)₂ peak in the HPLC chromatogram in the presence of HU not only suggests that HU can successfully neutralize the substrate-based radical but also that the substrate radical can exit the active site to be quenched by HU, evidenced by the inability of HU to induce spectral shifts in the UV-vis spectrum and the absence of competitive binding in the Lineweaver-Burk (LB) plots. Although HU can quench the substrate radical, it does not allow us to observe the radical intermediate directly. Thus, we turned to spin-traps.

Our first attempts using a common nitrone spin-trap, 5,5dimethyl-1-pyrroline-N-oxide (DMPO), did not lead to the detection of any DMPO-adducts via HPLC, which is typically observed when trapping a radical (Figure S12).35 We then recruited nitrosobenzene (NB), a nitroso-based spin trap capable of capturing a radical during enzymatic oxidation,. 35-3 Titrating TyrH with NB resulted in a red-shift of the Soret band to 416 nm, along with the emergence of new α/β bands at 561 and 540 nm, respectively (Figure S13A). These spectral changes are not only similar to NB bound to hemoglobin,³⁸ but also indicate NB binding ($K_D = 296 \pm 8 \mu M$) (Figure S13B). Upon the addition of excess H_2O_2 , UV-vis spectroscopy reveals a long-lived intermediate at 306 nm that populates and decays over time (Figure 6, A & B) with unique absorbance not seen in the NB UV-vis spectrum (Figure S14). By plotting the difference spectra and monitoring at 306 nm after adding excess hydrogen peroxide and NB, it is apparent that the intermediate is only present with NB, and not with L-Tyr or HPPA (Figure S15).

During the course of the reaction, the 306 nm peak maximizes in 2 min and gradually dissipates within 30 min (Figure 6B, inset). EPR spectroscopy confirms a NB radical (Figure 6C, (ii), which was not detected in the absence of the enzyme (Figure S16). The free radical signal exhibited a similar increase and decrease during freeze-thaw cycles, indicating its stability within a 5 min period before significant decay occurred over 30 min. Regrettably, no oxygenated or dimeric products were detected, suggesting the essential role of the phenolic oxygen (i.e., the 4-hydroxyl group) in the substrate during catalysis for oxygenation or oxidative dimerization completion (Figure S17). The spin-localization of the nitroso group of NB appears to hinder free radical coupling for dimerization, leading to the gradual degradation of the NB radical species over time. However, attempts to employ NB as a spin trap in L-Tyr oxidation were unsuccessful in detecting a new radical signal. This outcome may be attributed to the fact that the L-Tyr-based radical either does not kinetically accumulate or the heme distal pocket lacks sufficient space to accommodate an NB molecule following the arrival of an L-Tyr substrate. Furthermore, when HPPA is titrated into the

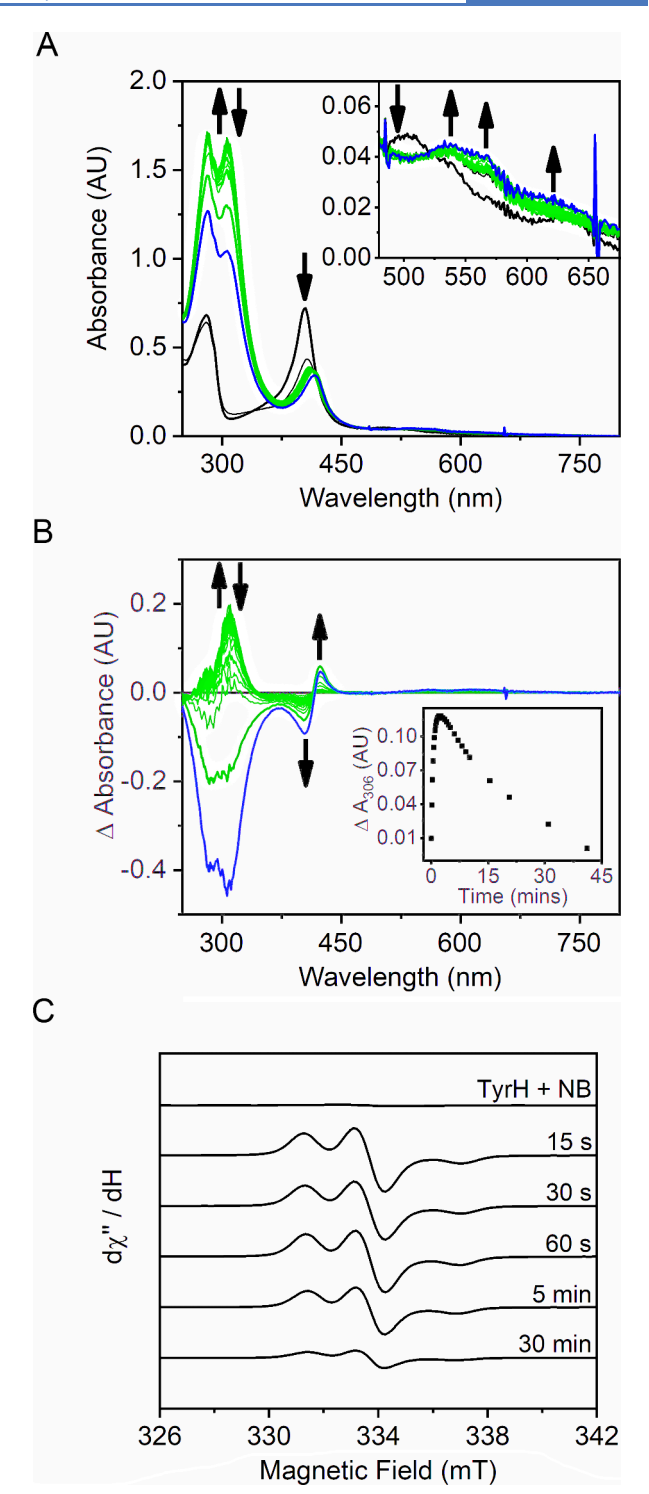


Figure 6. Characterization of a long-lived radical with NB. (A) UV—vis spectra of 10 $\mu\rm M$ TyrH (black trace) mixed with 30 eq. of $\rm H_2O_2$ (thin black), then 30 eq. of NB (thick green). The thick blue line is the same sample measured the following day, and intermediate spectra are drawn as thin green lines. (B) The difference spectrum of panel A, which was generated by subtracting the initial spectrum collected after the addition of hydrogen peroxide and NB (thin green trace in panel A) from subsequent spectra. The inset plots the change in absorbance at 306 nm over time. (C) EPR spectra of the low-spin region of TyrH-NB complex (top trace) and after incubation with 30 eq of $\rm H_2O_2$ for 15 s, 30 s, 60 s, 5 min, and 30 min. The EPR spectra were recorded at 30 K.

Scheme 2. Proposed Mechanistic Scheme of TyrH with HPPA

"Once the radical-based intermediate is produced, the pathway diverges to either perform oxidative aromatic C-H bond cleavage, generating the expected DHCA product or a (HPPA)₂.

TyrH-NB complex in the presence of excess hydrogen peroxide, the intensity of the NB-derived radical signal is progressively diminished (Figure S18). This observation supports the interpretation that HPPA and NB compete for access to a common oxidizing equivalent, likely a high-valent heme-based intermediate.

DISCUSSION

This study provides compelling evidence that the hemedependent tyrosine hydroxylase proceeds its monooxygenation process through a peroxidase-like pathway via a substratebased free radical intermediate. Three key findings substantiate this conclusion. First, the detection of (HPPA)₂ alongside the hydroxylated DHCA product suggests a radical-based coupling of the alternate substrate in catalysis. Second, the radical scavenger HU effectively eliminates HPPA dimerization, further supporting a radical mechanism. Third, direct spectroscopic observation of a nitrosobenzene-based radical species, when used as a substitute analog, provides direct experimental validation of a radical-based intermediate. While a substrate-based radical has been proposed computationally for IDO and TDO in the form of Fe(III)-O-O-(L-Trp), experimental confirmation has remained elusive. Here, for the first time, we establish a radical-based mechanism in TyrH, a member of the heme-dependent HDAO superfamily. These findings not only redefine the catalytic paradigm of TyrH but also suggest a potentially conserved radical mechanism across the diverse and biomedically significant HDAO superfamily, which spans thousands of enzymes involved in primary aromatic amino acid metabolism or secondary metabolism for natural product biosynthesis.

The crystal structure and spectroscopic data collectively demonstrate that HPPA binds to the active site of TyrH in a manner analogous to L-Tyr. Consequently, it is reasonable to infer that HPPA and L-Tyr undergo similar oxidation processes

mediated by TyrH. Furthermore, the observation of hydroxylated HPPA, DHCA, coupled with oxygen scrambling at the phenolic position of DHCA provides confirmation for such expectation. The formation of (HPPA)₂ is attributed to an intermediate, most likely a substrate-based radical, which is less efficient in completing the subsequent O-atom insertion step and migrates out of the enzyme. In contrast, NB can bind in the active site when used as an alternate substrate, and a free radical was observed as expected. However, the spin-trapping properties of NB concomitant with the lack of a hydroxyl group critical for catalysis 14 prevent the formation of a NB product. Notably, this lack of product detection is not unprecedented. No NB product was obtained in previous work involving radical trapping with the diheme peroxidase MauG.³⁷ It is also worth noting that the mechanism of radical formation on NB fundamentally differs from L-Tyr and HPPA. Whereas L-Tyr and HPPA undergo proton-coupled electron transfer (PCET) to generate neutral radicals, NB is more likely to yield a cationic radical species in the presence of a highvalent iron species. Nonetheless, the NB probe depicts that a radical can be formed with an alternate substrate. Although product was not detected in the presence of NB, the observed radical, in conjunction with the data presented in this body of work, supports the formation of a radical-based intermediate during catalysis by TyrH.

HU clearly inhibits the formation of (HPPA)₂ and, to a lesser extent, DHCA, as demonstrated by both HPLC and UV-vis spectroscopy. Attempts to analyze this inhibition using LB plots yielded no discernible trends (Figure S19), suggesting that the mechanism cannot be easily classified as competitive, noncompetitive, or uncompetitive inhibition. Rather, we propose that a unique inhibition takes place where HU attenuates dimer formation outside the active site due to the limited space within the active site. While HU primarily prevents the dimerization of HPPA, a small amount can enter

the active site to inhibit the hydroxylation of HPPA to DHCA, as evidenced by HPLC and UV-vis data.

The investigation using the substrate analog HPPA reveals the contribution of the amino group and underscores the essential catalytic role of the phenol moiety. Our previous ¹⁸Olabeling experiments with 3-F-L-Tyr have suggested a dearomatized intermediate. 13 Additionally, a hydroperoxo intermediate has also been captured in crystallo complexed with 3-F-L-Tyr. 14 The dimerization product observed with HPPA supports a radical-based dearomatized intermediate, potentially a ketone radical (Scheme 2). The previously identified active site base, His88, forms a crucial hydrogen bond with the substrate phenol, as further supported by computational chemistry. ^{14,16} An independent QM/MM study not only suggests the implications of intrinsic electric fields in catalysis but also supports the formation of a substrate radical and cpd II, 15 aligning with our previous and current findings. Without the phenol group, hydroxylation cannot take place, as is evident with NB.

Our proposed mechanism begins with the binding of HPPA to the distal pocket of the heme center (Scheme 2). In the presence of H₂O₂, cpd 0 is formed. The subsequent cleavage of the terminal oxygen, coupled with a PCET initiated by His88, results in the oxidation of the substrate, leaving a neutral radical. At this juncture, oxygen scrambling and two mechanistic pathways unfold. One pathway involves the ferryl-oxo group attacking the radicalized intermediate, leading to an iron-bound L-DOPA-quinone-like intermediate and the eventual formation of hydroxylated product. The alternative pathway involves recombining radicalized intermediates, resulting in (HPPA)2. Once the radical leaves the active site in the presence of excess HU, it is quenched. It is unlikely that the formation of the dimer takes place in the active site due to the spatial constraints (Figure S20). The proposed mechanistic scheme for the hydroxylation of L-Tyr can be found in Scheme S1. One subtle distinction is the detection of a small fraction of low-spin species by EPR and resonance-enhanced Raman spectroscopy. This likely arises because, in the presence of L-Tyr, the pK_a of the weakly coordinated water is lowered, leading to its partial conversion into hydroxide—a strong-field ligand, as observed in resonance Raman studies of TDO. 40 The divergence in pathways appears dependent on the longevity of the substrate radical, with both pathways sharing the initial steps of the classic heme peroxidase catalytic cycle up to the formation of cpd II.41

TyrH is a member of the HDAO superfamily; therefore, it is anticipated that similar catalytic mechanisms will be shared within this superfamily. The other well-characterized members, IDO and TDO, have been proposed to utilize a substrate-based radical during the formation of an alkyl peroxo intermediate that connects the heme iron with the L-Trp substrate. ^{22–24,42,43} However, such a substrate radical intermediate has yet to be experimentally observed. This work presents for the first time that a member of the HDAO superfamily generates a free radical on its bound substrate.

Briefly, our results underscore the nonessential but important role of the amino group in the substrate, facilitating the O-atom transfer from the heme-bound oxidant to the substrate in the TyrH reaction. Removing the amino group of tyrosine with HPPA disrupted the hydrogen bonding network, allowing us to examine the importance of these interactions. However, this could have unintentionally altered the mechanism. Formation of the hydroxylated product with

HPPA confirmed that the mechanism remains consistent with that of tyrosine. In the absence of this amino group, as demonstrated by HPPA, the oxidation reaction struggles to complete hydroxylation. The α -amino group of L-Tyr is postulated to contribute to the stabilization of the keto-radical intermediate by anchoring it within the active site (Scheme S1). In the cpd 0 intermediate, the α -amino group is positioned 2.8 and 3.0 Å from the proximal and distal peroxo oxygen atoms, respectively. 14 This proximity suggests a plausible role in maintaining the intermediate within the active site, thereby promoting formation of the dopaquinone-like intermediate. Alternatively, the α -amino group may lower the activation barrier for hydroxylation, a possibility that warrants further computational investigation. The amino group in L-Trp has been demonstrated in TDO through computational and experimental investigations to facilitate the second oxygen atom transfer. 22,24,44-46 Because the amino group plays an important role in both monocygenation and dioxygenation in TyrH and TDO, respectively, it is not the single determining factor differentiating between the two reactions in this superfamily.

Although TyrH and TDO/IDO belong within the same family and their oxidation pathways appear to proceed through substrate-radical intermediates, which is now confirmed by this work, they exhibit notable structural and mechanistic differences. First, they act on distinct aromatic substrates. To date, the only other known tyrosine utilizing-enzymes in this family are SfmD⁴⁷ and the newly discovered RhzB.⁴⁸ How this structure-based family differentiates between phenol and indole rings remains an open question. Second, TDO/IDO undergo two cycles of oxygenation while TyrH requires only one. Interestingly, MarE, a tryptophan-utilizing enzyme in this family, can perform both monooxygenation and dioxygenation. 48,49 However, the factors driving this differentiation remain unclear. Although this body of work confirms that the amino group is not the key factor governing substrate or oxygenation differentiation, the underlying causes of these differences remain unknown and warrant further investigation.

CONCLUSION

This study highlights the critical yet nuanced role of the α amino group in heme-dependent tyrosine hydroxylase catalysis. In the presence of this group, the enzyme channels reactivity toward efficient hydroxylation, whereas its absence, modeled with HPPA, permits an alternative radical-mediated dimerization pathway. Through a combination of structural biology, isotopic labeling, spectroscopy, and radical-trapping experiments, we provide experimental evidence for a substrate-based free radical intermediate—an observation that had long been postulated but never confirmed in the HDAO superfamily. These findings establish that while the amino group is not absolutely required for catalysis, it exerts an influence on reaction fidelity by stabilizing the substrate radical and promoting productive O-atom transfer. This mechanistic insight not only advances our fundamental understanding of radical chemistry in metalloenzymes but also opens avenues for engineering oxygenase reactivity in biocatalysis and natural product biosynthesis.

MATERIALS AND METHODS

Material Preparation. TyrH from *S. sclerotialus* with a *N*-terminal His₆-tag was expressed in *E. coli* cells and purified

using affinity chromatography as previously described. ¹⁴ Untagged protein was prepared by incubating it with TEV protease overnight and further purified using affinity and size exclusion chromatography, as previously reported. ¹⁴ L-Tyr and HPPA were purchased from Sigma-Aldrich at the highest purity while nitrosobenzene came from MP Biomedicals. Hydroxyurea was purchased from Acros Organics. 5,5-dimethyl-1-pyrroline *N*-oxide (DMPO) was purchased from Cayman Chemical (Ann Arbor, MI, USA).

Spectroscopic Characterization. All UV-vis spectra were recorded in a 1 cm quartz cuvette using either a Lambda 25 spectrophotometer (PerkinElmer) with a scan speed of 240 nm/s or an Agilent 8453 UV-vis spectrophotometer. All samples were measured in 100 mM potassium phosphate with 50 mM NaCl at pH 7.4, unless otherwise stated. The inset of Figure 5 was fitted to a hyperbolic model.

EPR spectra were recorded at either 10 or 30 K on a Bruker E560 X-band spectrometer equipped with a cryogen-free 4 K system controlled with an ITC503S temperature controller (Oxford Instruments, Abingdon, UK) and an SHQE-W resonator at 100 kHz modulation frequency, 0.6 mT modulation amplitude, and 1.002 mW power. The free radical signal was quantified by measuring 1 mM of $\rm CuSO_4$ in 10 mM EDTA buffered at pH 8.0. The double integration of the cupric signal represented 1 mM. The double integration of the radical signal was divided by that of the copper signal to estimate the quantity.

Resonance Raman spectra were obtained at an excitation line of 406.7 nm from a Kr⁺ ion laser (Coherent Innova 300C, Santa Clara, CA) directed toward an NMR tube seated on a spinning turbine. The scattered light, collected at a 90° angle to the incident laser beam, was focused on the 100-µm wide entrance slit of an IsoPlane SCT320 spectrometer equipped with a 1200 grooves/mm grating (Princeton Instruments, Trenton, NJ), where it was dispersed and then detected by an air cooled PIXIS CCD (charge coupled devices) detector (Princeton Instruments, Trenton, NJ). A long pass filter (Thorlabs, Newton, NJ) removed the laser scattering. The Raman shift was calibrated by using indene (Sigma). The laser power was kept at 20 mW for all measurements. The acquisition time was 20 min for all spectra obtained.

Reaction with Alternate Substrate and Product **Identification.** The oxidation of HPPA by H_2O_2 in TyrHmediated reaction was conducted under the reported conditions at room temperature in 100 mM potassium phosphate with 50 mM NaCl at pH 8.0. 13,14 Briefly, 100 μ M TyrH was premixed with 3 mM HPPA for 5 min before the addition of 3 mM H₂O₂. Reactions with NB, DMPO, and HU contained 10 mM of each reagent. The reaction mixture was quenched by 10 μ L of 6 M HCl, filtered, and analyzed by HPLC. The products were purified using a C18 Inertsil ODS-3 C18 column (3 μ m particle size, 4.6 × 250 mm, GL Sciences Inc.) at a 1 mL/min flow rate. The stationary phase was 99.9% H₂O with 0.1% formic acid and the mobile phase was 99.9% acetonitrile with 0.1% formic acid. The gradient started 4 min after the run began, increasing from 0% to 100% mobile phase in 18 min. The fractions eluted from HPLC were collected and concentrated by a vacuum concentrator for further NMR analysis.

High-resolution mass spectra were collected on a maXis plus quadrupole-time-of-flight mass spectrometer equipped with an electrospray ionization source (Bruker Daltonics) and operated in negative ionization mode. Samples were analyzed from

HPLC fraction and introduced into the ESI source via a syringe pump at a constant flow rate of 3 μ L/min. Important source parameters are summarized as follows: capillary voltage, - 3500 V; nebulizer gas pressure, 0.4 bar; dry gas flow rate, 4.0 L/min; source temperature, 200 °C. Mass spectra were averages of one minute of scans collected at a rate of 1 scan per second in the $50 \le m/z \le 1500$ range. Compass Data Analysis software version 4.3 (Bruker Daltonics) processed all mass spectra. The method for ¹⁸O percentage calculations is described elsewhere.⁵⁰ Briefly, calculations were carried out based on the areas under the monoisotopic peaks of the compound in question. The third isotopic peak overlaps with the monoisotopic peak of the singly ¹⁸O labeled, increasing the overall peak area. A corrected area for the monoisotopic peak of the ¹⁸O labeled species was calculated by subtracting the contribution of the intensity-corrected third isotopic peak area from the singly ¹⁸O labeled. This process was repeated for doubly labeled ¹⁸O labeled products and so forth.

NMR spectra were recorded on a Bruker (Billerica, MA) Avance III HD 500 MHz spectrometer equipped with a 5 mm Cryoprobe Prodigy apparatus at 300 K. Spectra were recorded in 90/10 buffer/ D_2O . One-dimensional 1H spectra (zg30) were recorded with 1 s relaxation delay and 32,000 data points and multiplied with an exponential function for a line broadening of 0.3 Hz before Fourier transformation.

Phase-sensitive, multiplicity-edited, gradient-selected HSQC (Bruker pulse program hsqcedetgpsisp2.3) with ^{13}C decoupling during acquisition (GARP). Spectral widths: 12.98 ppm (^{1}H , F2) \times 199.78 ppm (^{13}C , F1). Acquired matrix: 2048 points (F2) \times 32 t_1 increments; 512 scans per increment; relaxation delay d_1 = 1.5 s. The one-bond delay was set for $^{1}\text{J}_{\text{CH}}$ = 145 Hz. Processed matrix (zero-filled): 2048 \times 2048.

Phase-sensitive, gradient-selected HMBC (Bruker pulse program hmbcetgpl3nd) with a 3-fold low-pass J-filter to suppress one-bond correlations and no heteronuclear decoupling during acquisition. Spectral widths: 12.98 ppm (1 H, F2) \times 239.49 ppm (13 C, F1). Nominal acquired matrix: 4096 points (F2) \times 32 t₁ increments; 512 scans per increment; relaxation delay d₁ = 2.0 s. The long-range delay was set for nJ_{CH} = 8 Hz (\approx 62.5 ms). Processed matrix (zero-filled): 4096 \times 2048. All 2D spectra were manually phase corrected and baselined. All NMR data were processed using MestReNova NMR v11.0.3 software.

Inhibition Kinetics and Lineweaver–Burk Plots. The samples were prepared by incubating TyrH (10 μ M) with 100, 200, and 300 μ M HPPA. HU (0.1, 0.2, 0.5, 1.0, and 5 mM) was added to the mixture before 0.3 mM of H₂O₂ was used to initiate the reaction and monitored by UV–vis spectroscopy. The UV–vis spectra were obtained at 30 s intervals for 5 min. The initial rates were determined, and the inverse rates were plotted against the inverse HPPA concentrations. The data points were then fitted to a linear equation.

Crystal Structure Determination of TyrH Bound with HPPA. Untagged TyrH was used for cocrystallization. HPPA (3 mM) was added to TyrH (40 mg/mL). The crystallization conditions were identical as the reported conditions. All crystals were cryoprotected with 25% (v/v) glycerol before flash-cooling. X-ray diffraction data collection was conducted at the beamline 19-BM of the Advance Photon Source at Structural Biology Center (SBC, Argonne National Laboratory) at 100 K. Diffraction imagines were collected sequentially ($\Delta \varphi = 0.5^{\circ}$, total of 240°) with an incident wavelength of 0.96682 Å. Each data set was obtained on a

distinct single crystal from one continuous data collection at the beamline. The data sets were processed by HKL3000 and solved by molecular replacement via Phaser-MR in Phenix.⁵¹ A coordinate of PDB 7KQR with heme and all ligands excluded was used as the search model for molecular replacement. Restraints for HPPA (Ligand ID HPP) were generated with SMILES string using eLBOW and used for fitting and refinement using Phenix.^{51,52} In order to minimize bias, ligand refinement was initiated at the final stage of structure refinement by examining ligand-omit difference maps.

ASSOCIATED CONTENT

Supporting Information

The Supporting Information is available free of charge at https://pubs.acs.org/doi/10.1021/acscatal.5c05776.

Additional data and figures including MS/MS fragmentation patterns, UV—vis and EPR spectroscopy, HPLC chromatography, superimposition of tyrosine-bound TyrH and TyrH-HPPA, X-ray data collection and refinement statistics of TyrH-HPPA, including Scheme S1, Figures S1 to S20, and Tables S1 to S4 (PDF) 3D structure of HPPA-bound TyrH (PDB) (CIF)

Accession Codes

The structural coordinates resulting from this work have been deposited in the PDB with an entry 8VMK.

AUTHOR INFORMATION

Corresponding Author

Aimin Liu — Department of Chemistry, University of Texas at San Antonio, San Antonio, Texas 78249, United States; orcid.org/0000-0002-4182-8176; Email: Feradical@utsa.edu

Authors

Ephrahime S. Traore — Department of Chemistry, University of Texas at San Antonio, San Antonio, Texas 78249, United States; Occid.org/0000-0001-6419-9248

Yifan Wang — Department of Chemistry, University of Texas at San Antonio, San Antonio, Texas 78249, United States; Department of Chemistry, University of Georgia, Athens, Georgia 30602, United States; orcid.org/0000-0003-0378-2469

Wendell P. Griffith – Department of Chemistry, University of Texas at San Antonio, San Antonio, Texas 78249, United States; Occid.org/0000-0003-2633-6103

Complete contact information is available at: https://pubs.acs.org/10.1021/acscatal.5c05776

Notes

The authors declare no competing financial interest.

ACKNOWLEDGMENTS

We thank Dr. Remigio Usai for the constructive discussion of resonance Raman results. This work was financially supported by a National Institute of General Medical Sciences (NIGMS) of the National Institutes of Health (NIH) grant GM108988 (to A.L.). E.T. and Y.W. acknowledge generous financial support from the NIH under award numbers GM145187 and GM147510, respectively. A.L. thanks the Lutcher Brown Endowment support. The NIH grant G12MD007591 supported the UTSA Mass Spectrometry & Proteomics Core

Facility. We thank Dr. Daniel Wherritt for helping with the 2D NMR analysis. The NMR facility was sponsored by the National Science Foundation (NSF) under award no. 1625963. We thank the staff scientists for their assistance with remote data collection at beamline 19-BM at the Argonne National Laboratory of Advanced Photon Source (APS). The US Department of Energy (DOE), Office of Science, and Office of Basic Energy Sciences under Contract DE-AC02-06CH11357 supported the use of the APS beamline.

ABBREVIATIONS

3-F-L-Tyr, 3-fluoro-L-tyrosine; 3-(4-hydroxyphenyl)propionic acid, HPPA; 6cHS, six-coordinate high spin; 6cLS, six-coordinate low spin; HDAO, heme dependent aromatic oxygenase; LB, Lineweaver—Burk; L-Trp, L-tryptophan; L-Tyr, L-tyrosine; NB, nitrosobenzene

REFERENCES

- (1) Naoi, M.; Parvez, H. Tyrosine Hydroxylase; Taylor & Francis, 1993.
- (2) Fitzpatrick, P. F. Mechanism of Aromatic Amino Acid Hydroxylation. *Biochemistry* **2003**, *42* (48), 14083–14091.
- (3) Hausinger, R. P. FeII/alpha-Ketoglutarate-dependent Hydroxylases and Related Enzymes. *Crit. Rev. Biochem. Mol. Biol.* **2004**, 39 (1), 21–68.
- (4) Rosenzweig, A. C.; Sazinsky, M. H. Structural Insights into Dioxygen-activating Copper Enzymes. *Curr. Opin. Struct. Biol.* **2006**, 16 (6), 729–735.
- (5) Wang, Y.; Liu, A. Carbon-Fluorine Bond Cleavage Mediated by Metalloenzymes. *Chem. Soc. Rev.* **2020**, 49 (14), 4906–4925.
- (6) Lyte, M. Microbial Endocrinology in the Pathogenesis of Infectious Disease. *Microbiol. Spectr.* **2016**, 4 (2), VMBF-0021-2015.
- (7) Yang, J.; Stuart, M. A. C.; Kamperman, M. Jack of All Trades: Versatile Catechol Crosslinking Mechanisms. *Chem. Soc. Rev.* **2014**, 43 (24), 8271–8298.
- (8) Nagatsu, T.; Levitt, M.; Udenfriend, S. Tyrosine Hydroxylase. The Initial Step in Norepinephrine Biosynthesis. *J. Biol. Chem.* **1964**, 239, 2910–2917.
- (9) Matoba, Y.; Kumagai, T.; Yamamoto, A.; Yoshitsu, H.; Sugiyama, M. Crystallographic Evidence That the Dinuclear Copper Center of Tyrosinase is Flexible During Catalysis. *J. Biol. Chem.* **2006**, 281 (13), 8981–8990.
- (10) Brahme, N. M.; Gonzalez, J. E.; Rolls, J. P.; Hessler, E. J.; Mizsak, S.; Hurley, L. H. Biosynthesis of the Lincomycins.1. Studies Using Stable Isotopes on the Biosynthesis of the Propyl-L-Hygric and Ethyl-L-Hygric Acid Moieties of Lincomycin-A and Lincomycin-B. J. Am. Chem. Soc. 1984, 106 (25), 7873–7878.
- (11) Hofer, I.; Crusemann, M.; Radzom, M.; Geers, B.; Flachshaar, D.; Cai, X. F.; Zeeck, A.; Piel, J. Insights into the Biosynthesis of Hormaomycin, An Exceptionally Complex Bacterial Signaling Metabolite. *Chem. Biol.* **2011**, *18* (3), 381–391.
- (12) Connor, K. L.; Colabroy, K. L.; Gerratana, B. A Heme Peroxidase with a Functional Role as an L-Tyrosine Hydroxylase in the Biosynthesis of Anthramycin. *Biochemistry* **2011**, *50* (41), 8926–8936.
- (13) Wang, Y. F.; Davis, I.; Shin, I.; Wherritt, D. J.; Griffith, W. P.; Dornevil, K.; Colabroy, K. L.; Liu, A. M. Biocatalytic Carbon-Hydrogen and Carbon-Fluorine Bond Cleavage through Hydroxylation Promoted by a Histidyl-Ligated Heme Enzyme. *ACS Catal.* **2019**, 9 (6), 4764–4776.
- (14) Wang, Y. F.; Davis, I.; Shin, I.; Xu, H.; Liu, A. M. Molecular Rationale for Partitioning between C-H and C-F Bond Activation in Heme-Dependent Tyrosine Hydroxylase. *J. Am. Chem. Soc.* **2021**, *143* (12), 4680–4693.
- (15) Peng, W.; Yan, S.; Zhang, X.; Liao, L.; Zhang, J.; Shaik, S.; Wang, B. How Do Preorganized Electric Fields Function in Catalytic

- Cycles? The Case of the Enzyme Tyrosine Hydroxylase. *J. Am. Chem. Soc.* **2022**, *144* (44), 20484–20494.
- (16) Singh, W.; Santos, S. F. G.; Yadav, S.; Black, G. W.; Dubey, K. D. Substrate Conformation Regulates Aromatic C-H Vs C-F Bond Activation in Heme-Dependent Tyrosine Hydroxylase. *Biochemistry* **2023**, *62* (10), 1577–1587.
- (17) Colabroy, K. L. Tearing Down to Build Up: Metalloenzymes in the Biosynthesis Lincomycin, Hormaomycin and the Pyrrolo [1,4]benzodiazepines. *Biochim. Biophys. Acta* **2016**, *1864* (6), 724–737.
- (18) Peschke, U.; Schmidt, H.; Zhang, H. Z.; Piepersberg, W. Molecular Characterization of the Lincomycin-production Gene Cluster of *Streptomyces lincolnensis* 78–11. *Mol. Microbiol.* **1995**, *16* (6), 1137–1156.
- (19) Li, W.; Chou, S.; Khullar, A.; Gerratana, B. Cloning and Characterization of the Biosynthetic Gene Cluster for Tomaymycin, an SJG-136 Monomeric Analog. *Appl. Environ. Microbiol.* **2009**, 75 (9), 2958–2963.
- (20) Li, W.; Khullar, A.; Chou, S.; Sacramo, A.; Gerratana, B. Biosynthesis of Sibiromycin, A Potent Antitumor Antibiotic. *Appl. Environ. Microbiol.* **2009**, 75 (9), 2869–2878.
- (21) Shin, I.; Wang, Y.; Liu, A. A New Regime of Heme-dependent Aromatic Oxygenase Superfamily. *Proc. Natl. Acad. Sci. U.S.A.* **2021**, 118 (43), No. e2106561118.
- (22) Shin, I.; Ambler, B. R.; Wherritt, D.; Griffith, W. P.; Maldonado, A. C.; Altman, R. A.; Liu, A. M. Stepwise O-Atom Transfer in Heme-Based Tryptophan Dioxygenase: Role of Substrate Ammonium in Epoxide Ring Opening. *J. Am. Chem. Soc.* **2018**, *140* (12), 4372–4379.
- (23) Capece, L.; Lewis-Ballester, A.; Yeh, S. R.; Estrin, D. A.; Marti, M. A. Complete Reaction Mechanism of Indoleamine 2,3-Dioxygenase as Revealed by QM/MM Simulations. *J. Phys. Chem. B* **2012**, *116* (4), 1401–1413.
- (24) Chung, L. W.; Li, X.; Sugimoto, H.; Shiro, Y.; Morokuma, K. ONIOM Study on a Missing Piece in Our Understanding of Heme Chemistry: Bacterial Tryptophan 2,3-Dioxygenase with Dual Oxidants. J. Am. Chem. Soc. 2010, 132 (34), 11993–12005.
- (25) Basran, J.; Efimov, I.; Chauhan, N.; Thackray, S. J.; Krupa, J. L.; Eaton, G.; Griffith, G. A.; Mowat, C. G.; Handa, S.; Raven, E. L. The Mechanism of Formation of N-Formylkynurenine by Heme Dioxygenases. J. Am. Chem. Soc. 2011, 133 (40), 16251–16257.
- (26) 3-(4-Hydroxyphenyl)propanoic acid NMR Spectrum. Available at: https://spectrabase.com/spectrum/5veQKA2JZs6.
- (27) Lindblad, B.; Lindstedt, G.; Lindstedt, S. The Mechanism of Enzymic Formation of Homogentisate from *p*-Hydroxyphenylpyruvate. *J. Am. Chem. Soc.* **1970**, 92 (25), 7446–7449.
- (28) Hu, S. Z.; Smith, K. M.; Spiro, T. G. Assignment of protoheme Resonance Raman spectrum by heme labeling in myoglobin. *J. Am. Chem. Soc.* **1996**, *118* (50), 12638–12646.
- (29) Terentis, A. C.; Thomas, S. R.; Takikawa, O.; Littlejohn, T. K.; Truscott, R. J.; Armstrong, R. S.; Yeh, S. R.; Stocker, R. The Heme Environment of Recombinant Human Indoleamine 2,3-Dioxygenase. Structural Properties and Substrate-Ligand Interactions. *J. Biol. Chem.* **2002**, 277 (18), 15788–15794.
- (30) Lu, C.; Egawa, T.; Mukai, M.; Poole, R. K.; Yeh, S. R. Hemoglobins From *Mycobacterium tuberculosis* and *Campylobacter jejuni*: A Comparative Study with Resonance Raman Spectroscopy. *Methods Enzymol.* **2008**, 437, 255–286.
- (31) Greene, B. L.; Kang, G.; Cui, C.; Bennati, M.; Nocera, D. G.; Drennan, C. L.; Stubbe, J. Ribonucleotide Reductases: Structure, Chemistry, and Metabolism Suggest New Therapeutic Targets. *Annu. Rev. Biochem.* **2020**, *89*, 45–75.
- (32) Li, J. S.; Davis, I.; Griffith, W. P.; Liu, A. M. Formation of Monofluorinated Radical Cofactor in Galactose Oxidase through Copper-Mediated C-F Bond Scission. *J. Am. Chem. Soc.* **2020**, *142* (44), 18753–18757.
- (33) Lassmann, G.; Thelander, L.; Gräslund, A. EPR stopped-flow studies of the reaction of the tyrosyl radical of protein R2 from

- ribonucleotide reductase with hydroxyurea. Biochem. Biophys. Res. Commun. 1992, 188 (2), 879–887.
- (34) Reichard, P.; Ehrenberg, A. Ribonucleotide reductase-a radical enzyme. *Science* **1983**, 221 (4610), 514–519.
- (35) Liu, A.; Jin, Y.; Zhang, J.; Brazeau, B. J.; Lipscomb, J. D. Substrate Radical Intermediates in Soluble Methane Monooxygenase. *Biochem. Biophys. Res. Commun.* **2005**, 338 (1), 254–261.
- (36) Mottley, C.; Trice, T. B.; Mason, R. P. Direct detection of the sulfur trioxide radical anion during the horseradish peroxidase-hydrogen peroxide oxidation of sulfite (aqueous sulfur dioxide). *Mol. Pharmacol.* **1982**, 22 (3), 732–737.
- (37) Davis, I.; Koto, T.; Liu, A. Radical Trapping Study of the Relaxation of bis-Fe(IV) MauG. React. Oxyg. Species (Apex) 2018, 5 (13), 46–55.
- (38) Hirota, K.; Itano, H. A. Influence of Ring Substituents on the Binding of Nitrosobenzene by Ferrohemoglobin. *J. Biol. Chem.* **1978**, 253 (10), 3477–3481.
- (39) Geeraerts, Z.; Ishigami, I.; Gao, Y.; Yeh, S.-R. Heme-based dioxygenases: Structure, function and dynamics. *J. Inorg. Biochem.* **2024**, *261*, 112707.
- (40) Batabyal, D.; Yeh, S. R. Human Tryptophan Dioxygenase: A Comparison to Indoleamine 2,3-dioxygenase. *J. Am. Chem. Soc.* **2007**, 129 (50), 15690–15701.
- (41) Meunier, B.; de Visser, S. P.; Shaik, S. Mechanism of Oxidation Reactions Catalyzed by Cytochrome p450 Enzymes. *Chem. Rev.* **2004**, 104 (9), 3947–3980.
- (42) Lewis-Ballester, A.; Batabyal, D.; Egawa, T.; Lu, C. Y.; Lin, Y.; Marti, M. A.; Capece, L.; Estrin, D. A.; Yeh, S. R. Evidence for a Ferryl Intermediate in a Heme-based Dioxygenase. *Proc. Natl. Acad. Sci. U.S.A.* **2009**, *106* (41), 17371–17376.
- (43) Capece, L.; Lewis-Ballester, A.; Batabyal, D.; Di Russo, N.; Yeh, S. R.; Estrin, D. A.; Marti, M. A. The First Step of the Dioxygenation Reaction Carried Out by Tryptophan Dioxygenase and Indoleamine 2,3-Dioxygenase as Revealed by Quantum Mechanical/Molecular Mechanical Studies. *J. Biol. Inorg. Chem.* **2010**, *15* (6), 811–823.
- (44) Nakagawa, M.; Watanabe, H.; Kodato, S.; Okajima, H.; Hino, T.; Flippen, J. L.; Witkop, B. A Valid Model for the Mechanism of Oxidation of Tryptophan to Formylkynurenine-25 Years Later. *Proc. Natl. Acad. Sci. U.S.A.* **1977**, 74 (11), 4730–4733.
- (45) Davydov, R. M.; Chauhan, N.; Thackray, S. J.; Anderson, J. L.; Papadopoulou, N. D.; Mowat, C. G.; Chapman, S. K.; Raven, E. L.; Hoffman, B. M. Probing the Ternary Complexes of Indoleamine and Tryptophan 2,3-Dioxygenases by Cryoreduction EPR and ENDOR Spectroscopy. *J. Am. Chem. Soc.* **2010**, *132* (15), 5494–5500.
- (46) Booth, E. S.; Basran, J.; Lee, M.; Handa, S.; Raven, E. L. Substrate Oxidation by Indoleamine 2,3-Dioxygenase: Evidence for a Common Reactions Mechanism. *J. Biol. Chem.* **2015**, 290 (52), 30924–30930.
- (47) Shin, I.; Davis, I.; Nieves-Merced, K.; Wang, Y.; McHardy, S.; Liu, A. A Novel Catalytic Heme Cofactor in SfmD with a Single Thioether Bond and a bis-His Ligand Set Revealed by a de novo Crystal Structural and Spectroscopic Study. *Chem. Sci.* **2021**, *12* (11), 3984–3998.
- (48) Ehinger, F. J.; Niehs, S. P.; Dose, B.; Dell, M.; Krabbe, J.; Pidot, S. J.; Stinear, T. P.; Scherlach, K.; Ross, C.; Lackner, G.; Hertweck, C. Analysis of Rhizonin Biosynthesis Reveals Origin of Pharmacophoric Furylalanine Moieties in Diverse Cyclopeptides. *Angew. Chem. Int. Edit* 2023, 62 (42), No. e202308540.
- (49) Shin, I.; Nguyen, R. C.; Montoya, S. R.; Liu, A. Structural Insights into 2-Oxindole-forming Monooxygenase MarE: Divergent Architecture and Substrate Positioning versus Tryptophan Dioxygenases. *J. Biol. Chem.* **2025**, *301*, 108241.
- (50) Celic, I.; Masumoto, H.; Griffith, W. P.; Meluh, P.; Cotter, R. J.; Boeke, J. D.; Verreault, A. The Sirtuins Hst3 and Hst4p Preserve Genome Integrity by Controlling Histone H3 Hysine 56 Deacetylation. *Curr. Biol.* **2006**, *16* (13), 1280–1289.
- (51) Adams, P. D.; Afonine, P. V.; Bunkoczi, G.; Chen, V. B.; Davis, I. W.; Echols, N.; Headd, J. J.; Hung, L. W.; Kapral, G. J.; Grosse-Kunstleve, R. W.; McCoy, A. J.; Moriarty, N. W.; Oeffner, R.; Read, R.

- J.; Richardson, D. C.; Richardson, J. S.; Terwilliger, T. C.; Zwart, P. H. PHENIX: A Comprehensive Python-based System for Macromolecular Structure Solution. *Acta Crystallogr. D Biol. Crystallogr.* **2010**, *66* (2), 213–221.
- (52) Minor, W.; Cymborowski, M.; Otwinowski, Z.; Chruszcz, M. HKL-3000: The Integration of Data Reduction and Structure Solution-From Diffraction Images to an Initial Model in Minutes. *Acta Crystallogr. D Biol. Crystallogr.* **2006**, 62 (8), 859–866.

Supporting Information

Substrate Analogs Implicate a Free Radical Pathway in Tyrosine Hydroxylase Catalysis

Ephrahime S. Traore§, Yifan Wang§,‡, Wendell P. Griffith§, and Aimin Liu§,*

§Department of Chemistry, University of Texas at San Antonio, San Antonio, Texas 78249, U.S.A.

*Correspondence to:

Aimin Liu, Department of Chemistry, University of Texas at San Antonio, 1 UTSA Circle, San Antonio, TX 78249-0698; Phone: +1-210-458-7062; Fax: 210-458-7428; and E-mail: Feradical@utsa.edu

[‡]Department of Chemistry, University of Georgia, Athens, Georgia 30602, U.S.A.

TABLE OF CONTENTS

Table S1. 1H-NMR and 13C-NMR chemical shifts for (HPPA)2	S3
Table S2. Comparison of the ¹⁸ O-labeled unreacted substrate and hydroxylated product	S4
Table S3. Distribution of the 180-labeled dimerized product	S4
Table S4. X-ray data collection and refinement statistics of TyrH-HPPA	S5
Scheme S1. Proposed mechanistic scheme of TyrH with L-Tyr	S6
Figure S1. ¹ H NMR spectrum of HPPA	
Figure S2. ¹ H NMR spectrum of DHCA	S8
Figure S3. ¹ H NMR spectrum of (HPPA) ₂	S9
Figure S4. Superimposed 2D NMR spectra of (HPPA) ₂	S10
Figure S5. MS/MS fragmentation spectra on all TyrH products	S11
Figure S6. Oxygen scrambling sites for HPPA, DHCA, and (HPPA) ₂	S12
Figure S7. Spectroscopic characterization of TyrH bound to tyrosine and HPPA	S13
Figure S8. LB plot of TyrH bound with either HPPA or tyrosine	S14
Figure S9. Superimposed X-ray crystallography of TyrH-HPPA and TyH-tyrosine	S15
Figure S10. UV-vis spectra of TyrH mixed with hydroxyurea	
Figure S11. Monitoring reaction of TyrH-HPPA in the presence of HU	S17
Figure S12. Activity assay with DMPO	S18
Figure S13. Spectroscopic characterization of TyrH bound to nitrosobenzene	S19
Figure S14. UV-vis spectra of nitrosobenzene.	S20
Figure S15. UV-vis spectra of TyrH-HPPA and TyrH-tyrosine with excess H ₂ O ₂	S21
Figure S16. EPR spectra of NB and TyrH with and without excess H ₂ O ₂	S22
Figure S17. HPLC chromatogram of TyrH reaction with nitrosobenzene	S23
Figure S18. Room temperature EPR of TyrH-NB with various concentrations of HPPA in excess H ₂ O ₂	S24
Figure S19. Lineweaver Burk Plot with hydroxyurea as an inhibitor	S25
Figure \$20 Surface view of the TurH_HPPA complex active site	\$26

Table S1. ¹H-NMR and ¹³C-NMR chemical shifts for (HPPA)₂

Label	$\delta_{ m H}$	$\delta_{ extsf{C}}$
α	2.56 (t, J = 7.4, 2H)	29.45
β	2.88 (t, <i>J</i> = 7.4 Hz, 1H)	35.75
1	N/A	132.91
2	7.14 (d, J = 2.3 Hz, 1H)	131.05
3	N/A	125.23
4	N/A	151.23
5	6.96 (d, J = 8.3 Hz, 1H)	115.91
6	7.21 (dd, $J = 8.3$ Hz, 2.2 Hz, 1H)	129.14
7	N/A	178.21

Table S2. Comparison of the $^{18}\text{O-Labeled}$ Unreacted Substrate and Hydroxylated Product after the TyrH Reaction Using L-Tyr and HPPA in $^{18}\text{O-enriched}$ H $_2\text{O}$

		Unreacted Substrate			Hydroxylation				
Substrate	¹⁸ O atom in- corporation	0 180	1 180	2 180	0 180	1 180	2 180	3 ¹⁸ 0	4 180
L-Tyr ¹²	88%				87.7 ± 0.9	11.2 ± 0.8	1.0 ± 0.1		
НРРА	90%	32.9 ± 19.0	59.6 ± 22.9	7.5 ± 4.1	3.8 ± 0.2	22.1 ± 1.0	42.0 ± 0.7	26.6 ± 1.3	5.5 ± 0.7

Table S3. Distribution of the $^{18}\text{O-Labeled}$ Dimerized Product after the TyrH Reaction Using HPPA in $^{18}\text{O-enriched}$ H $_2\text{O}$

Dimerization							
Substrate	¹⁸ 0 atom incor- poration	O 18	1 ¹⁸ 0	2 180	3 ¹⁸ 0	4 180	5 ¹⁸ 0
НРРА	90%	18.1 ± 2.5	37.2 ± 1.4	30.0 ± 1.6	12.1 ± 1.7	2.4 ± 0.5	0.2 ± 0.06

Table S4. X-ray Data Collection and Refinement Statistics

	HPPA-bound binary complex
Data Collection	
Wavelength (Å)	0.96682
Space group	P 2 ₁
Cell dimensions	
a, b, c (Å)	47.63, 129.82, 48.42
α, β, γ (°)	90.00, 93.86, 90.00
Resolution (Å)	50.00 - 1.56
	(1.59 - 1.56)a
Total reflections	402617
Unique reflections	82562
Redundancy	4.9 (4.3)
R _{sym} or R _{merge} ^b (%)	7.8 (49.1)
CC _{1/2} c	95.8 (80.9)
Ι/σΙ	21.3 (2.0)
Completeness (%)	99.4 (98.9)
Refinement	
Resolution (Å)	48.31 - 1.56
No. reflections	82515
$R_{\rm work}^{\rm d}/R_{\rm free}^{\rm e}$ (%)	18.8 / 21.3
No. Atoms / B -factors (Å ²)	
Protein	4711 / 25.3
Heme	86 / 22.5
Ligands	40 / 26.5
Water	580 / 35.0
r.m.s.d	
Bond lengths (Å)	0.007
Bond angles (°)	0.984
Ramachandran ^f	
Favored (%)	97.3
Allowed (%)	2.5
Outlier (%)	0.2

PDB Code ^aNumbers in parentheses refer to data in the highest resolution shell.

8VMK

 $^{{}^}bR_{merge}$ = $\Sigma |I_h - \langle I_h \rangle|/\Sigma |I_h \rangle$, where I_h is the observed intensity and $\langle I_h \rangle$ is the average intensity.

^cAccording to Engh and Huber (1).

 $^{{}^{}d}R_{\text{work}} = \Sigma ||F_{\text{obs}}| - k|F_{\text{cal}}|| / \Sigma |F_{\text{obs}}|$

 $^{^{}e}R_{free}$ is the same as R_{obs} for a selected subset (10%) of the reflections that were not included in prior refinement calculations.

^fCalculated by using MolProbity (2).

gThe outlier in 8VMK is from Gly16 in chain A. This residue is from the surface flexible region and irrelevant to the active site.

^{1.} Engh, R. A., and Huber, R. (1991) Accurate bond and angle parameters for X-ray protein structure refinement. Acta Crystallogr. A 47, 392-400

^{2.} Chen, V. B., Arendall, W. B., 3rd, Headd, J. J., Keedy, D. A., Immormino, R. M., Kapral, G. J., Murray, L. W., Richardson, J. S., and Richardson, D. C. (2010) MolProbity: all-atom structure validation for macromolecular crystallography. Acta Crystallogr. D Biol. Crystallogr. 66, 12-21

Scheme S1. Proposed mechanistic scheme of TyrH with L-Tyr.

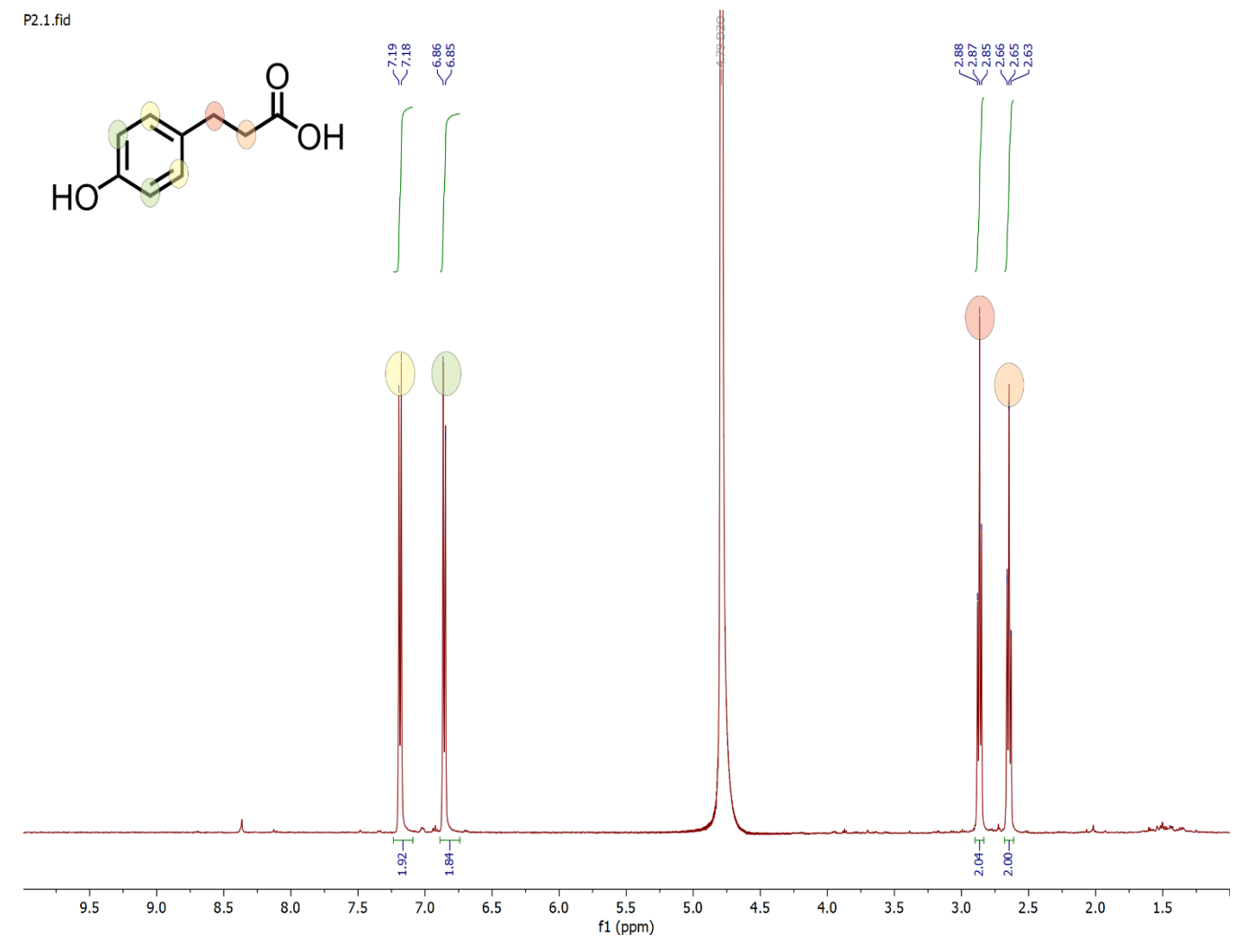


Figure \$1. Proton NMR spectrum of HPPA.

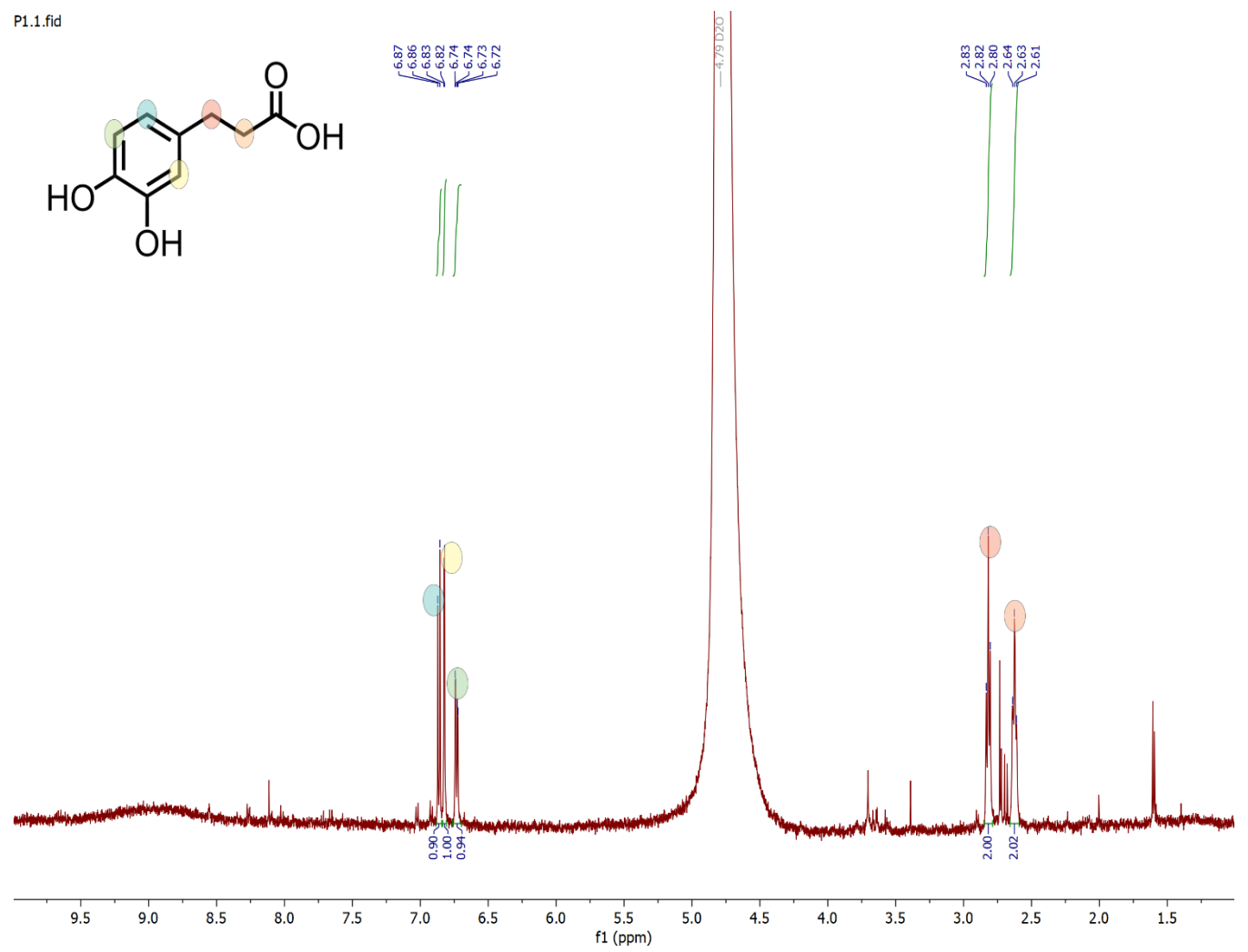


Figure S2. Proton NMR spectrum of DHCA.

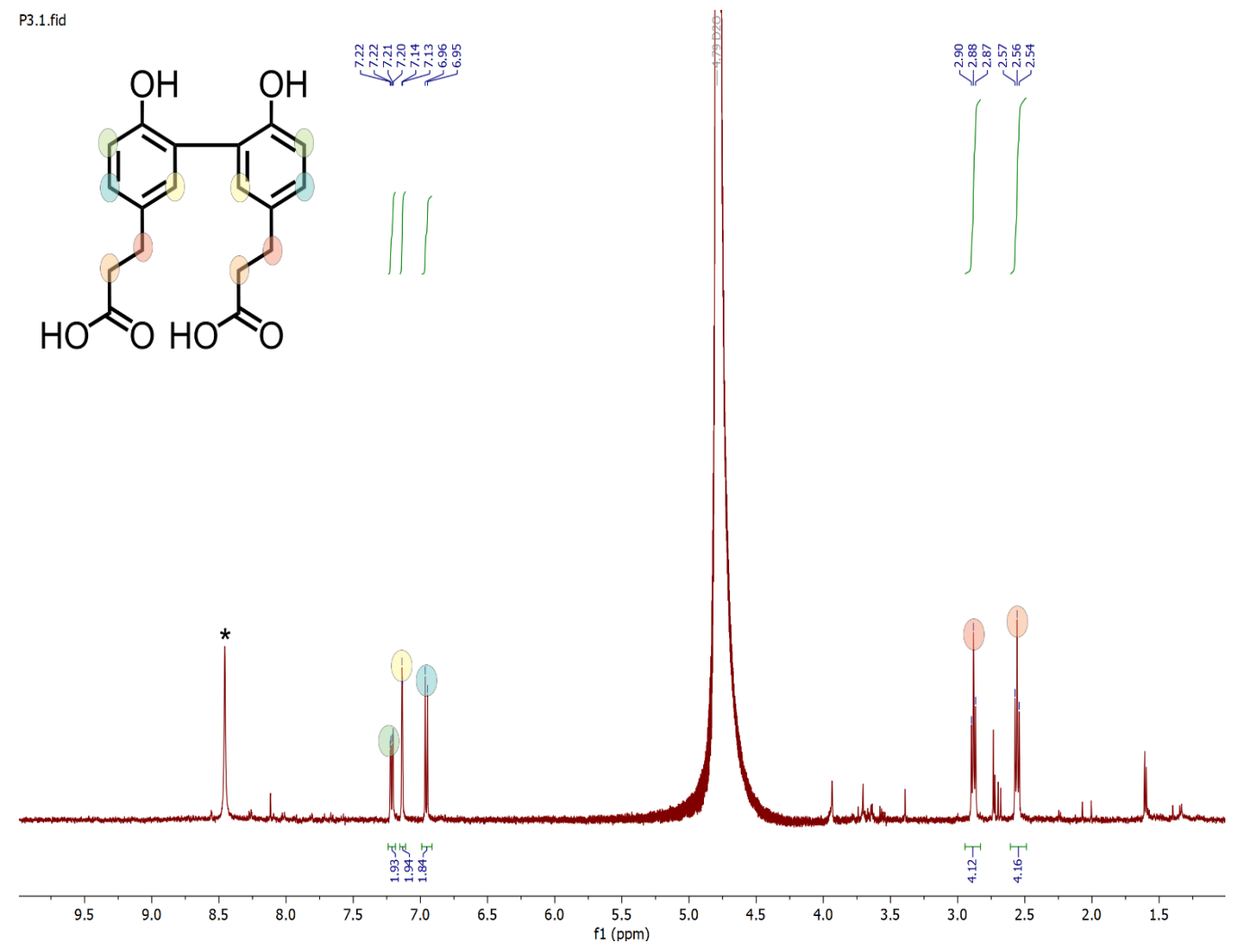


Figure S3. Proton NMR spectrum of (HPPA)2. The asterick represents formic acid that was present in the HPLC solvent.

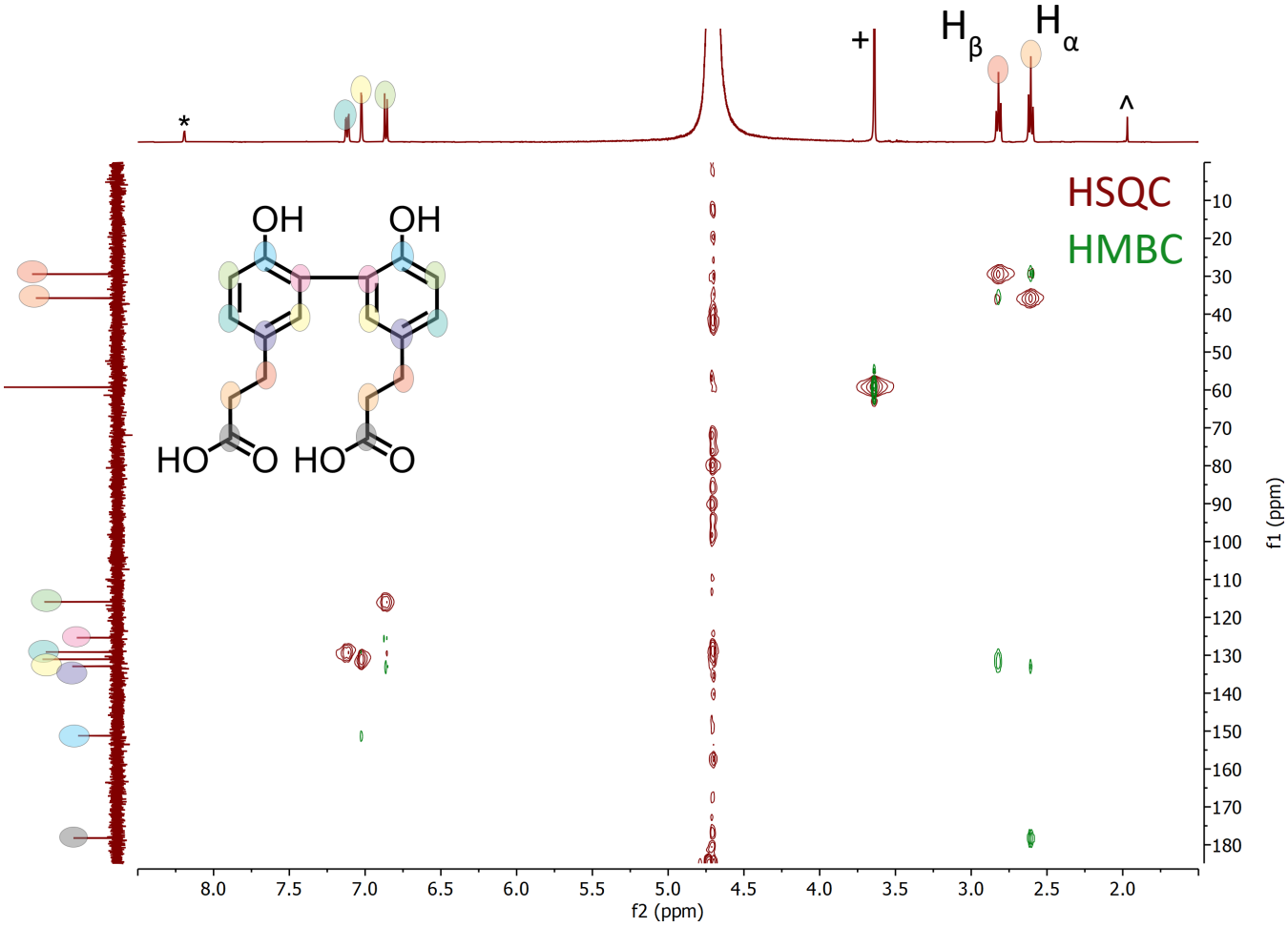


Figure S4. Superimposed 2D NMR of (HPPA)₂. HSQC is shown in maroon, while HMBC is shown in green. Formic acid, acetonitrile, and an unknown impurity is present and marked in the 1H NMR with a * , $^\wedge$, and $^+$, respectively.

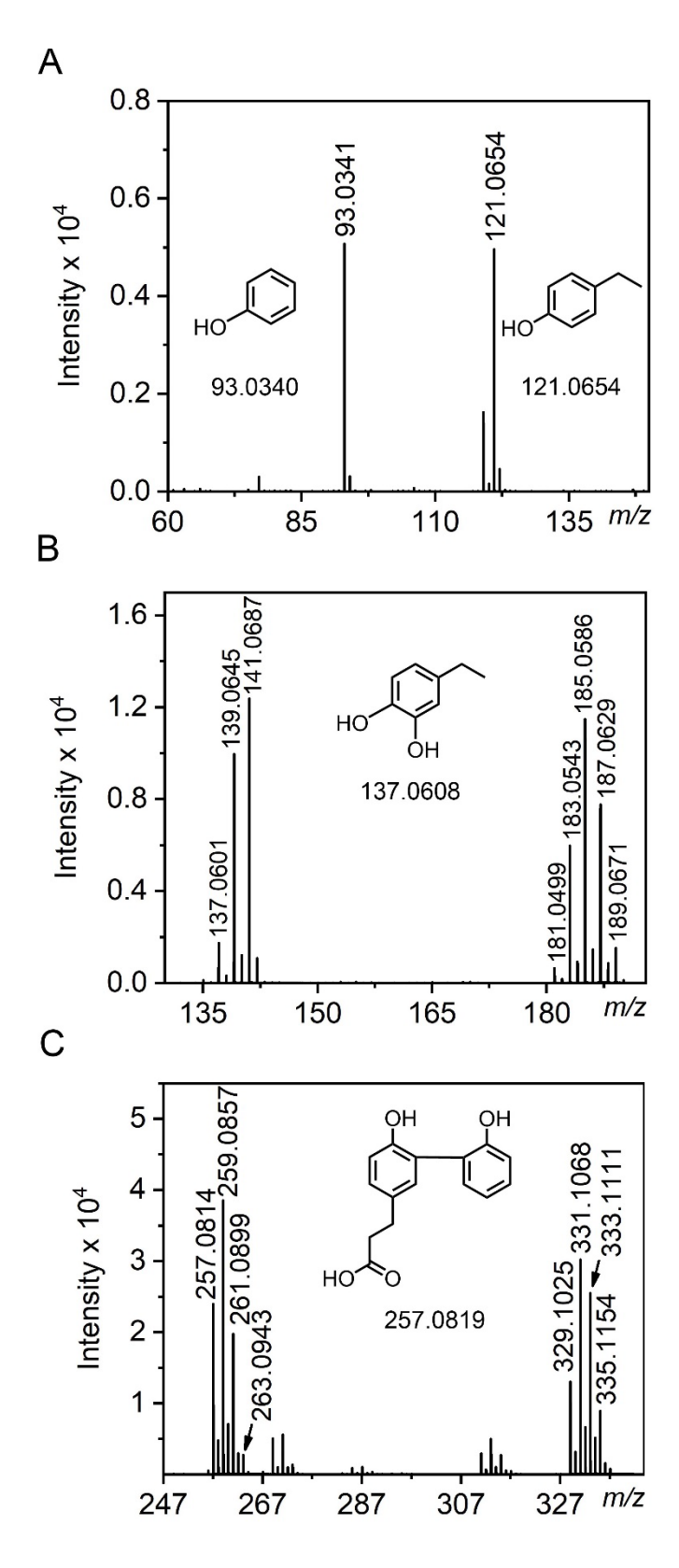


Figure S5. MS/MS fragmentation spectra of HPPA (A), DHCA (B), and (HPPA)₂ (C).

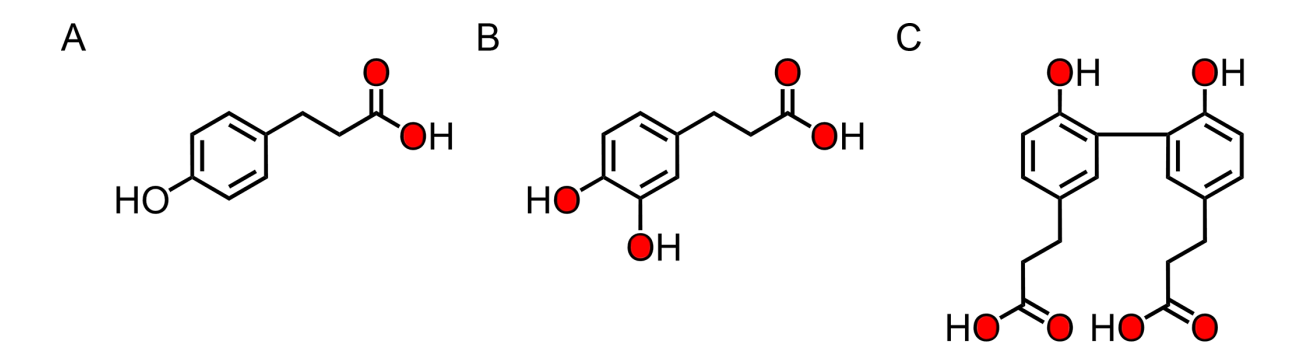


Figure S6. Oxygen exchange sites for (A) HPPA alone, whose phenolic oxygen does not exchange with solvent, (B) TyrH-mediated enzymatic reaction product DHCA, and (C) TyrH-mediated enzymatic reaction product (HPPA)₂.

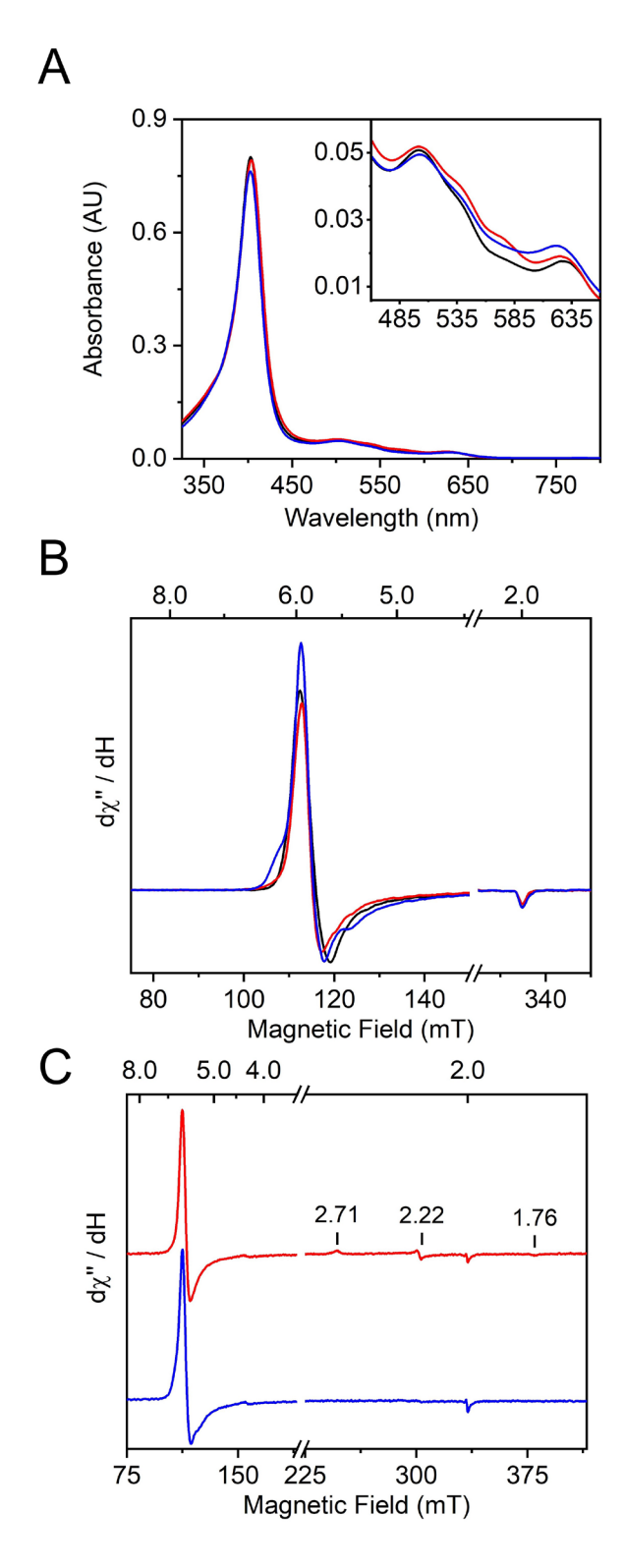


Figure S7. Spectroscopic studies of TyrH complex with L-Tyr and HPPA. (A) UV-vis spectra of 10 μ M TyrH (black), TyrH bound with 200 μ M L-Tyr (red) and TyrH bound with 200 μ M HPPA (blue). EPR spectra of 50 μ M TyrH (black) bound with 20 eq of L-Tyr (red) and HPPA (blue) at 10 K (B) and 30 K (C). All EPR spectra were recorded at 1 mW microwave power.

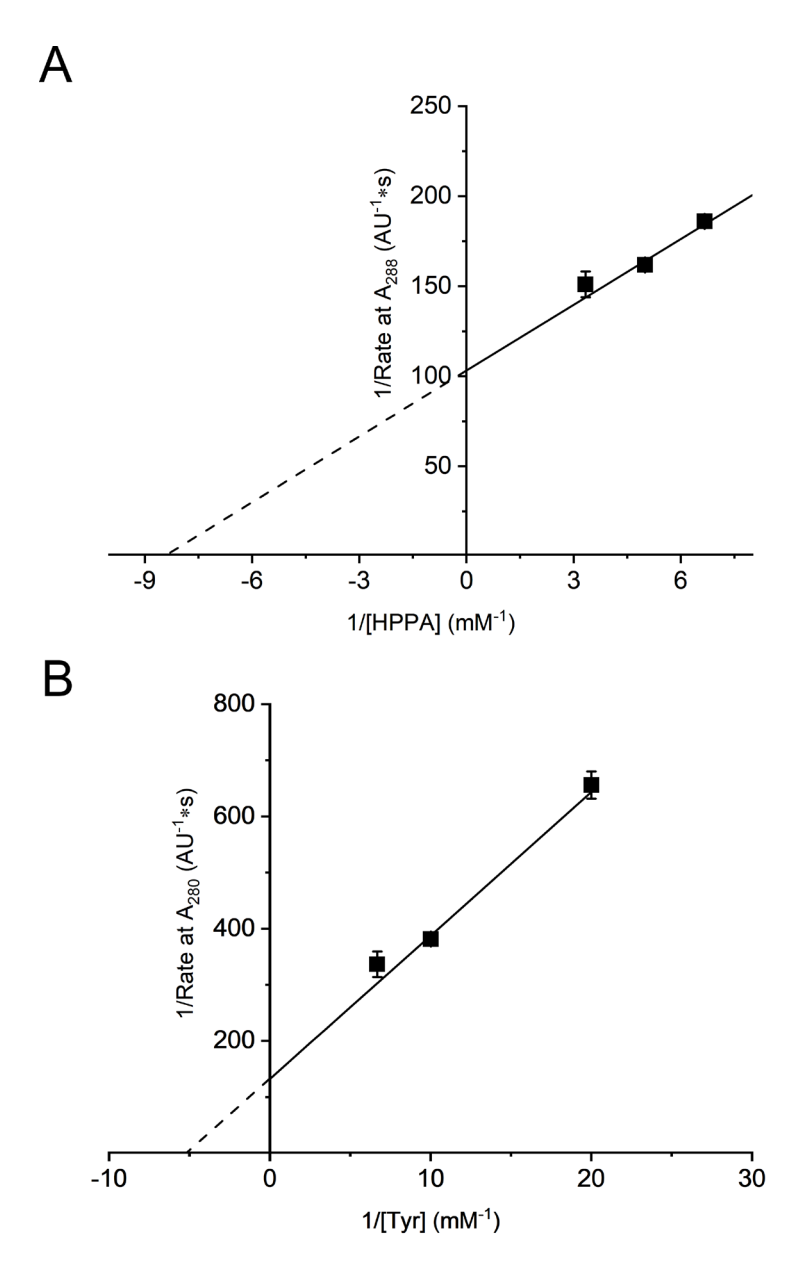


Figure S8. Lineweaver-Burk plot of TyrH bound with L-Tyr and HPPA. (A) The TyrH-HPPA reaction was monitored at 288 nm and (B) TyrH-Tyr reaction was monitored at 280 nm. 10 μ M TyrH was mixed with either 300 μ M HPPA or L-Tyr, and then 300 μ M of hydrogen peroxide was added to initiate the reaction. The initial rate was calculated and used to acquire the LB plot. The $K_{\rm M}$ and $V_{\rm max}$ for HPPA were determined to be 97 ± 37 μ M and 9 ± 1 mAU•s⁻¹ at 288 nm, and tyrosine was determined to be 111 ± 31 μ M and 5 ± 0.7 mAU•s⁻¹ at 280 nm.

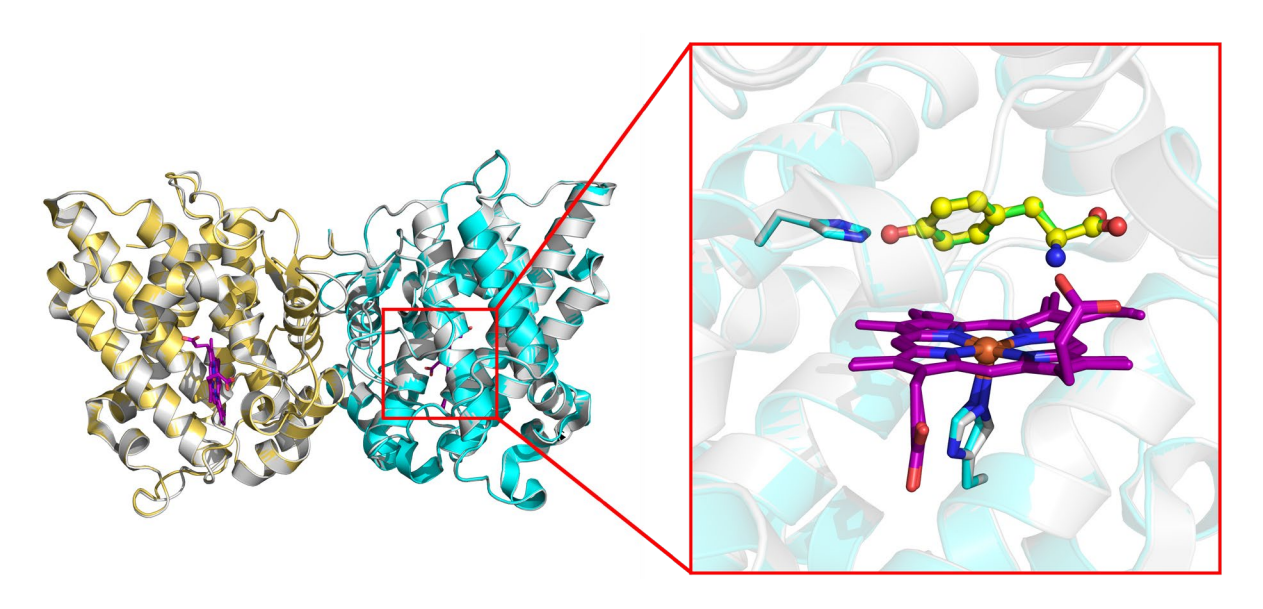


Figure S9. Superposition of the crystal structure of L-Tyr-bound TyrH (PDB ID: 7KQR) and TyrH-HPPA (PDB ID: 8VMK). The former is shown in grey, and the latter is colored with chain A in gold and chain B in light blue. The heme is drawn in purple sticks. The active site is zoomed in and shown on the right with L-Tyr drawn in yellow and HPPA in green ball and stick.

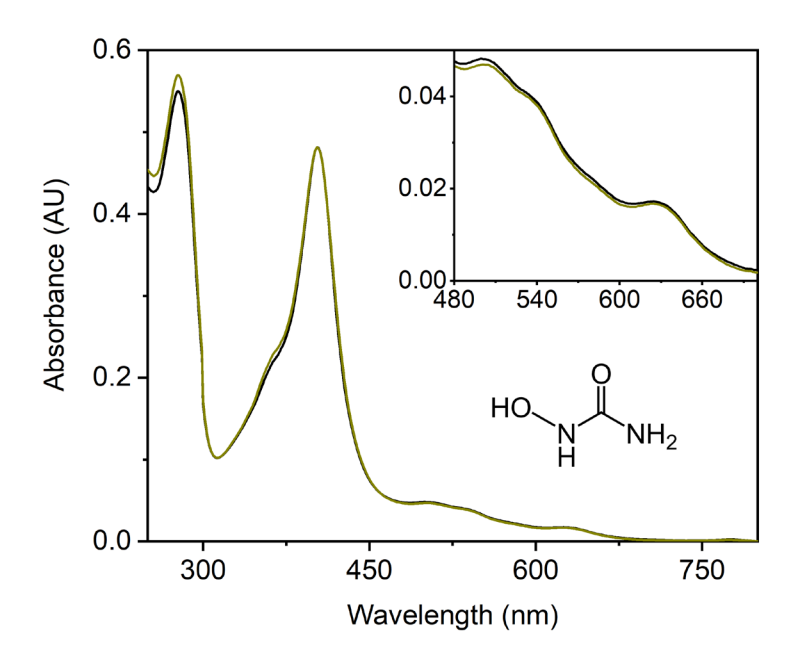
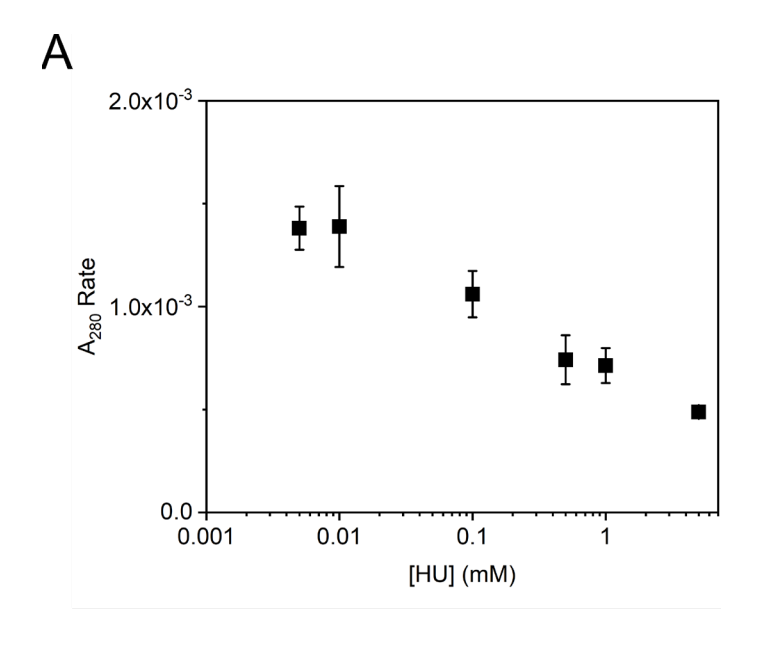


Figure S10. UV-vis spectra of TyrH (black) mixed with 1 mM HU (dark yellow). The chemical structure of hydroxyurea is also shown.



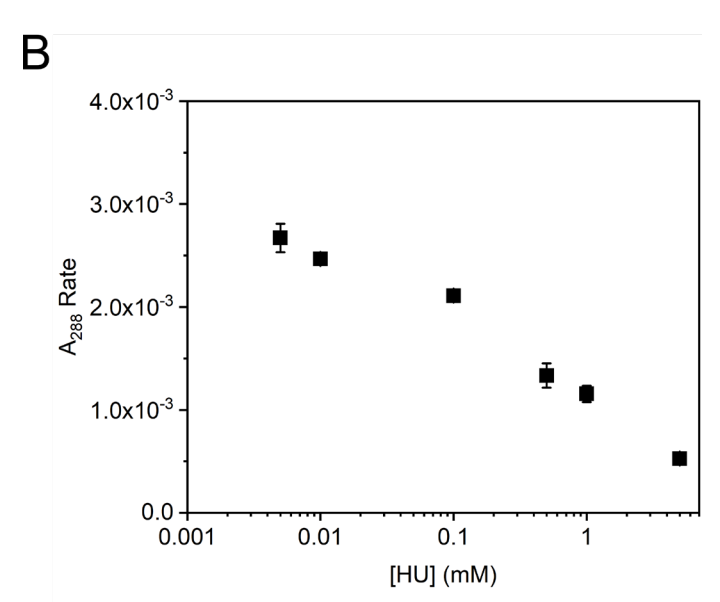


Figure S11. Activity assay of 10 μ M TyrH in the presence of 300 μ M HPPA 5 μ M, 10 μ M, 100 μ M, 500 μ M, 1 mM, and 5 mM of HU. (A) Depicts the rate of formation monitored at 280 nm and (B) is monitored at 288 nm.

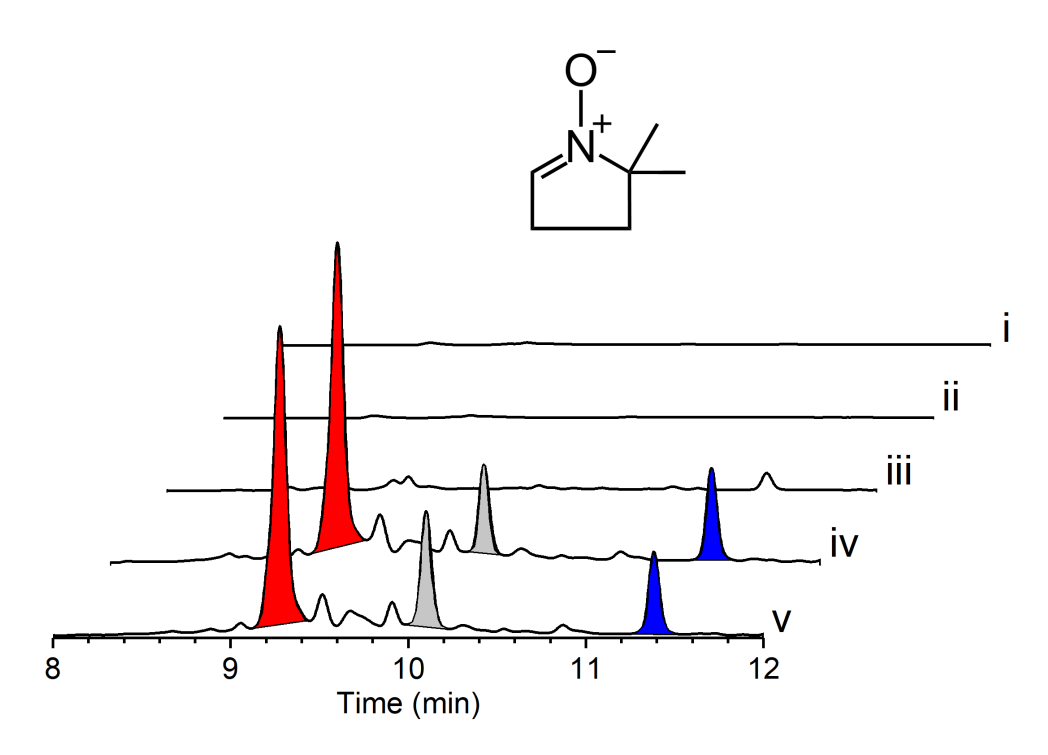


Figure S12. Activity assay with DMPO. (A) HPLC of (i) DMPO, (ii) DMPO mixed with H_2O_2 , (iii) TyrH incubated mixed with DMPO and H_2O_2 , (iv) TyrH-HPPA complex mixed with H_2O_2 , and (v) TyrH-HPPA complex mixed with DMPO and H_2O_2 . Peaks shaded in red, grey, and blue correspond to DHCA, HPPA, and (HPPA)₂, respectively. All chromatograms were monitored at 288 nm. The chemical structure of DMPO is shown at the top of the chromatogram.

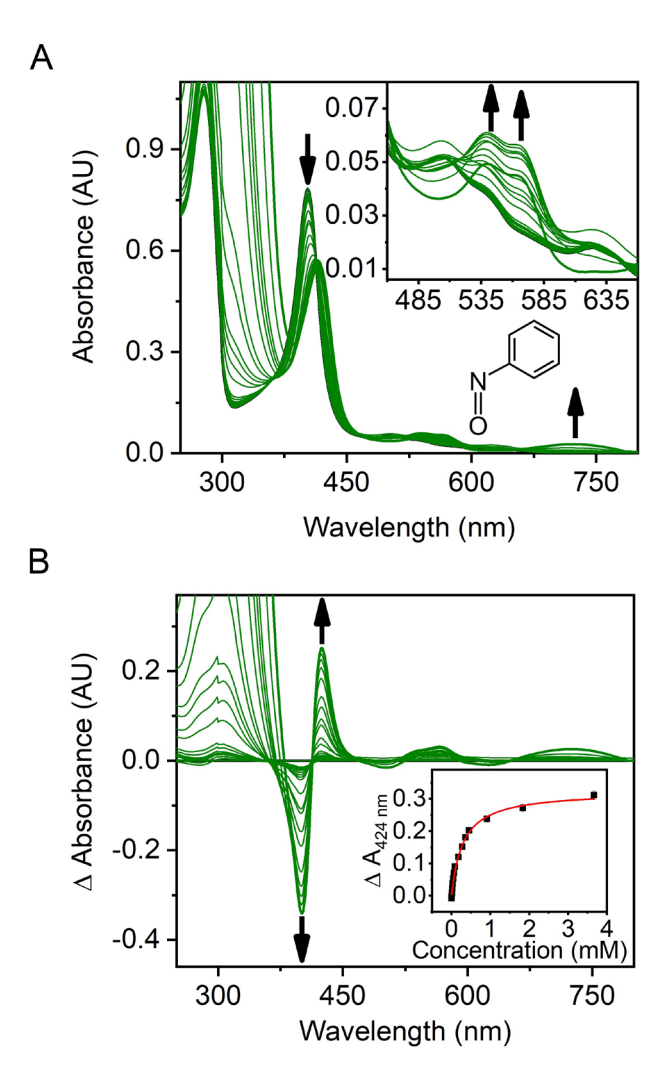


Figure S13. Spectroscopic characterization of TyrH bound to nitrosobezene (NB). (A) UV-vis spectra TyrH titrated with NB and the chemical structure of NB. (B) Difference spectra of panel A with the TyrH alone spectrum subtracted from each spectrum after the addition of NB. The inset depicts the difference spectra values at 424 nm plotted against the concentration of NB.

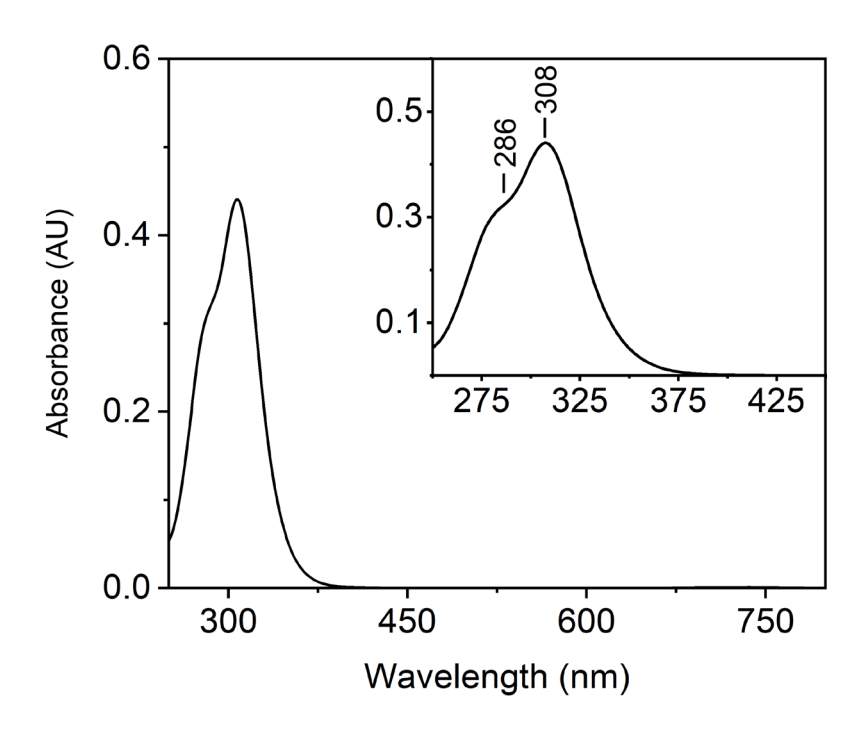


Figure S14. UV-vis spectrum of 100 μM nitrosobenzene.

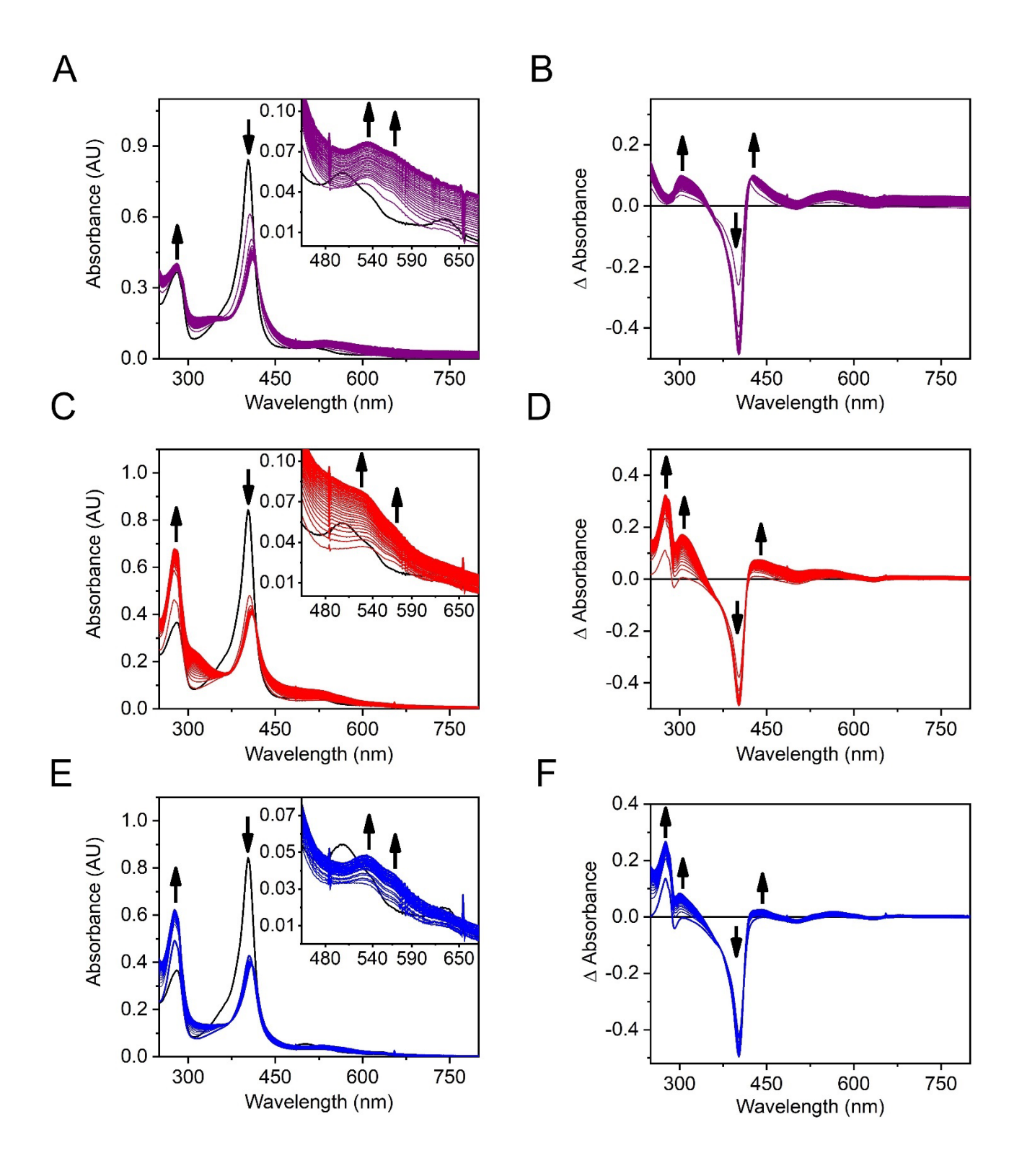


Figure S15. UV-vis time-dependent assays with TyrH with excess L-Tyr or HPPA and H_2O_2 over 30 min. (A) 10 μ M of TyrH (black trace) was mixed with 20 eq. of H_2O_2 and monitored over 30 min (purple trace). (B) Difference spectrum of panel A. (C) 10 μ M of TyrH with excess L-Tyr (black trace) was mixed with 20 eq. of H_2O_2 and monitored over 30 min (red trace). (D) Difference spectrum of panel C. (E) 10 μ M of TyrH with excess HPPA (black trace) was mixed with 20 eq. of H_2O_2 and monitored over time (blue trace). The final 30-min spectrum is a thick line with intermediary spectra shown in thin lines.

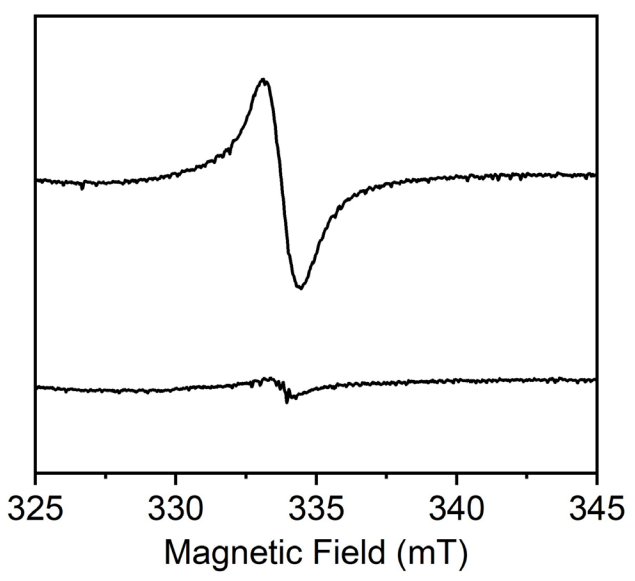


Figure S16. EPR spectra of 100 μ M TyrH with 30 eq. excess of H₂O₂ (top trace) and 100 μ M NB with 30 eq. of H₂O₂ (bottom trace). Both spectra were frozen after incubating for 30 s. The conditions are identical to that shown in Figure 6C.

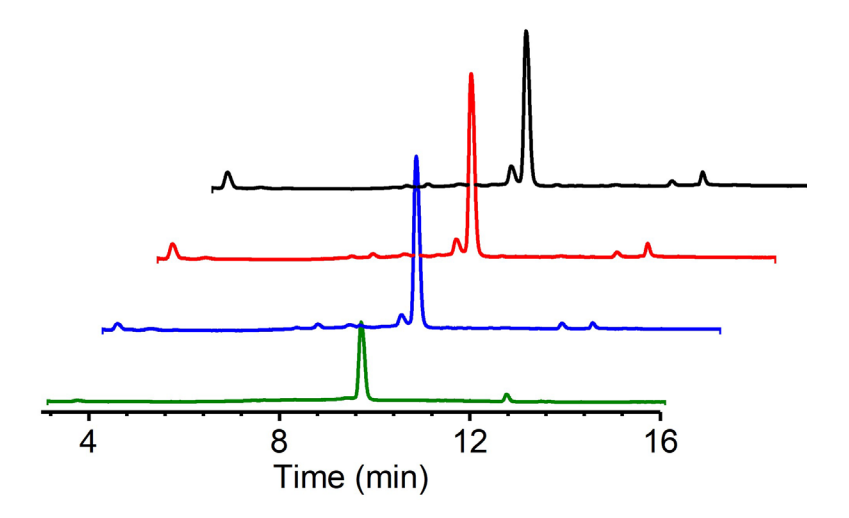


Figure S17. HPLC chromatogram of 100 μ M TyrH with 20 eq. excess of NB and H₂O₂. Each color represents a different wavelength, and the purification was monitored at various wavelengths, with black being 275 nm, red being 280 nm, 288 nm being blue, and 330 nm being green.

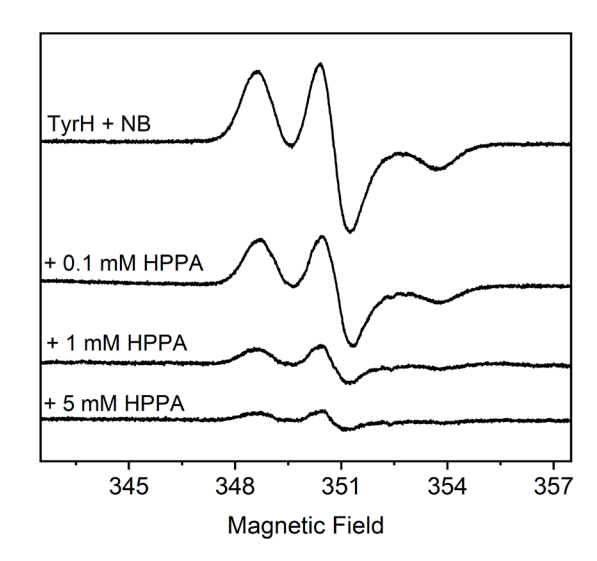


Figure S18. Room temperature EPR of 200 μ M TyrH in complex with 2.7 mM of nitrosobenzene, 1 mM of H₂O₂, and various concentrations of HPPA. The EPR spectra are an average of were obtained within 5 minutes of adding hydrogen peroxide and were recorded

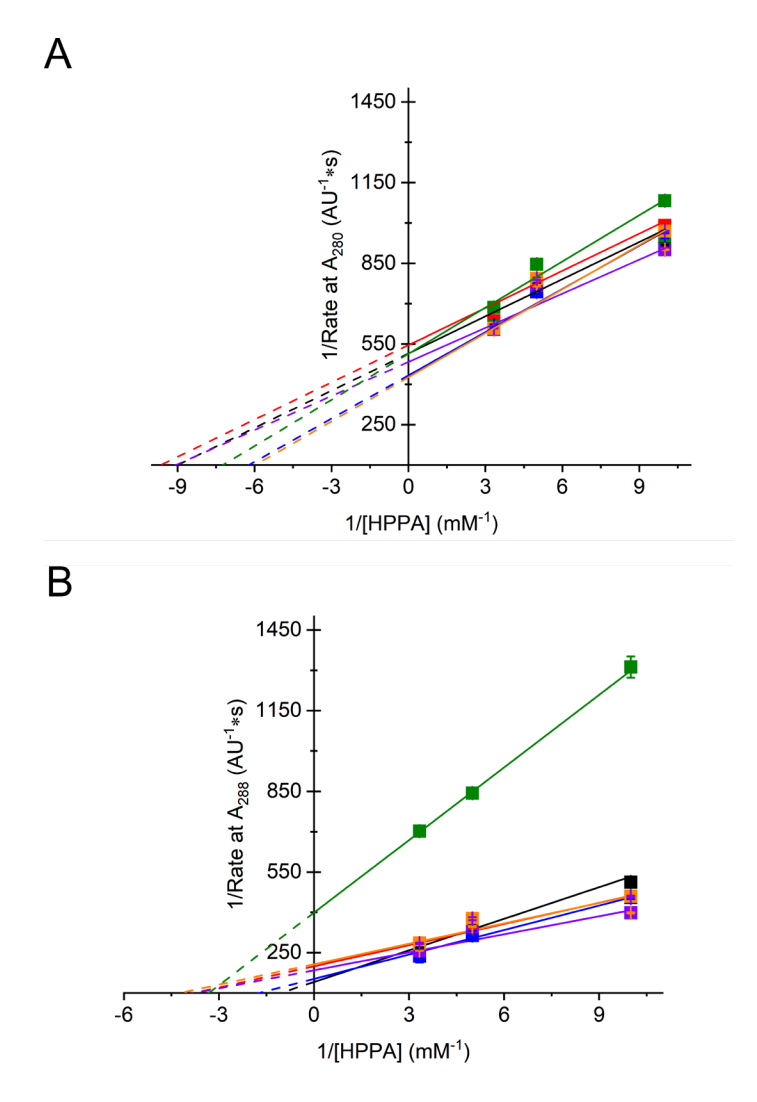


Figure S19. Lineweaver-Burk plot of Tyr-HPPA in the presence of 0 μ M (black trace), 100 μ M (red), 200 μ M (blue), 500 μ M (purple), 1 mM (orange), and 5 mM (green) HU monitored at 280 nm (A) and 288 nm (B). The solid line is the fitted line based on experimental values while the dashed represents hypothetical values. Experimental details can be found in the Materials and Methods.

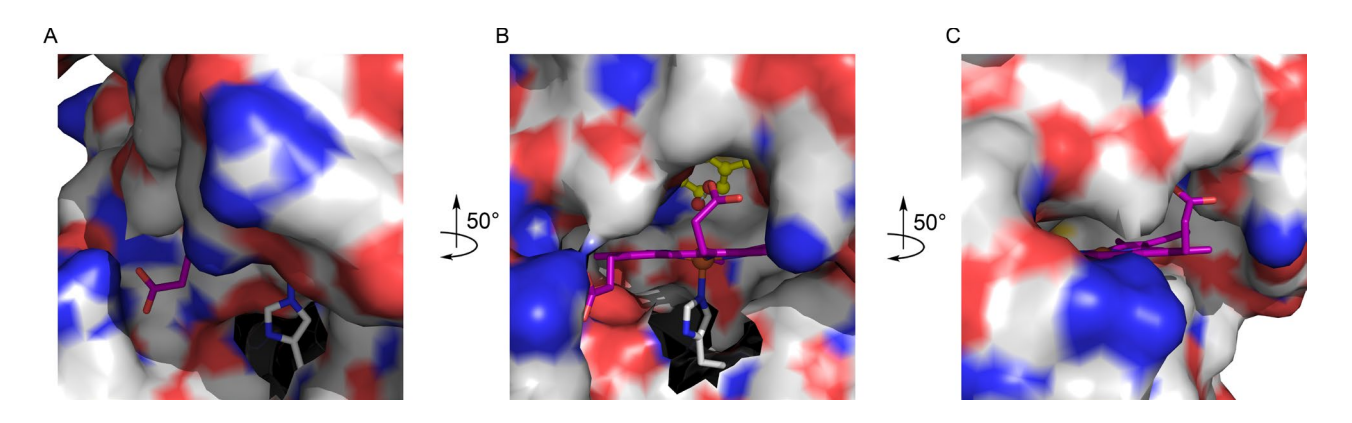


Figure S20. Surface view of the TyrH–HPPA complex active site with each panel rotated counterclockwise by 50 degrees to illustrate different orientations. Negatively charged surface residues are colored red, and positively charged residues are colored blue. The heme cofactor is depicted with magenta carbon atoms and a brown sphere representing the iron center. The bound substrate, HPPA, is shown as yellow sticks.